Low-Rankness Guided Group Sparse Representation for Image Restoration

Zhiyuan Zha, *Member, IEEE*, Bihan Wen, *Member, IEEE*, Xin Yuan, *Senior Member, IEEE*, Jiantao Zhou, *Senior Member, IEEE*, Ce Zhu, *Fellow, IEEE*, and Alex Chichung Kot, *Fellow, IEEE*

***Abstract*— As a spotlighted nonlocal image representation model, group sparse representation (GSR) has demonstrated a great potential in diverse image restoration tasks. Most of the existing GSR-based image restoration approaches exploit the nonlocal self-similarity (NSS) prior by clustering similar patches into groups and imposing sparsity to each group coefficient, which can effectively preserve image texture information. However, these methods have imposed only plain sparsity over each individual patch of the group, while neglecting other beneficial image properties, e.g., low-rankness (LR), leads to degraded image restoration results. In this article, we propose a novel low-rankness guided group sparse representation (LGSR) model for highly effective image restoration applications. The proposed LGSR jointly utilizes the sparsity and LR priors of each group of similar patches under a unified framework. The two priors serve as the complementary priors in LGSR for effectively preserving the texture and structure information of natural images. Moreover, we apply an alternating minimization algorithm with an adaptively adjusted parameter scheme to solve the proposed LGSR-based image restoration problem. Extensive experiments are conducted to demonstrate that the proposed LGSR achieves superior results compared with many popular or state-of-the-art algorithms in various image restoration tasks, including denoising, inpainting, and compressive sensing (CS).**

***Index Terms*— Adaptively adjusted parameter, alternating minimization, image restoration, low-rankness guided group sparse representation (LGSR), nonlocal self-similarity (NSS).**

Manuscript received July 27, 2021; revised November 6, 2021; accepted January 10, 2022. This work was supported in part by the Rapid-Rich Object Search (ROSE) Laboratory, Nanyang Technological University, Singapore; in part by the Ministry of Education, Republic of Singapore, through its Academic Research Fund Tier 1 under Project ID: RG137/20; in part by the Start-Up Grant; in part by the National Natural Science Foundation of China under Grant 62020106011, Grant U19A2052, and Grant 61971476; and in part by the Macau Science and Technology Development Fund, Macau, under Grant 077/2018/A2, Grant 0060/2019/A1, and Grant 0072/2020/AMJ. *(Corresponding author: Bihan Wen.)*

Zhiyuan Zha, Bihan Wen, and Alex Chichung Kot are with the School of Electrical and Electronic Engineering, Nanyang Technological University, Singapore 639798 (e-mail: zhiyuan.zha@ntu.edu.sg; bihan.wen@ntu.edu.sg; eackot@ntu.edu.sg).

Xin Yuan is with the School of Engineering, Westlake University, Hangzhou, Zhejiang 310024, China (e-mail: xyuan@westlake.edu.cn).

Jiantao Zhou is with the State Key Laboratory of Internet of Things for Smart City, and the Department of Computer and Information Science, University of Macau, Taipa, Macau 999078, China (e-mail: jtzhou@um.edu.mo).

Ce Zhu is with the School of Information and Communication Engineering, University of Electronic Science and Technology of China, Chengdu 611731, China (e-mail: eczhu@uestc.edu.cn).

This article has supplementary material provided by the authors and color versions of one or more figures available at https://doi.org/10.1109/TNNLS.2022.3144630.

Digital Object Identifier 10.1109/TNNLS.2022.3144630

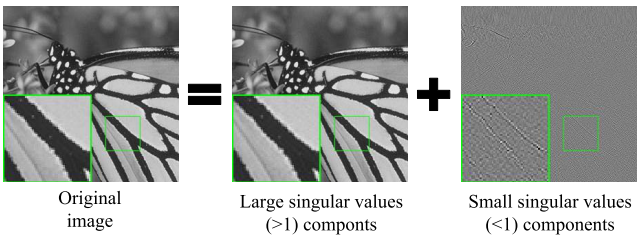

Fig. 1. Example image Monarch is decomposed into an image with large singular values and an image with small singular values. The non-low-rank (non-LR) (small singular) components contain important texture information of the image.

I. Introduction

It is well known that effective image priors play a substantial role in many ill-posed inverse problems [1]–[11]. The representative prior sparsity [2], [12], [13] argues that natural images are sparsifiable by certain dictionary or transform, which has been proven to be effective for various image restoration applications [14]–[17]. The classical sparsity models characterize each patch as a coefficient vector within a few nonzero elements in certain dictionary domains [2], [4], [18], [19]; meanwhile, others conduct adaptive sparsity in some transform domains [7], [20]. For instance, Elad and Aharon [2] learned an over-complete dictionary using the greedy algorithm to represent image patches. Wen *et al.* [7] proposed an effective image restoration method via the union of sparsity transform model. Nonetheless, most classical sparsity models employ the individual patch as the basic unit for sparse representation. They have only considered the local image structure but ignored the strong correlation among similar patches, such as self-similarity, especially the nonlocal ones [19], [21].

Via employing the nonlocal self-similarity (NSS) prior [21], [23] in images and clustering the nonlocal similar patches into groups, group sparse representation (GSR) [15] conducts each group for sparse representation, which has shown a great potential in image restoration studies [17], [19], [24]–[26]. For example, Dong *et al.* [24] designed a Laplacian-scale-mixture-based GSR model for image restoration. The so-called GSRC-NLP [17] enforced an effective group sparsity residual constraint, which has achieved a superior performance for various image restoration tasks. Zha *et al.* [4] established the connection between GSR and low-rank (LR) models by devising an adaptive dictionary. These mentioned GSR-based

Fig. 2. Image denoising results are achieved by our proposed LGSR and two state-of-the-art GSR and LR methods at a noise level of $\sigma_n = 30$. (a) Original image. (b) Noisy image. (c) GSRC-NLP [17] (31.19 dB). (d) Weighted nuclear norm minimization (WNNM) [22] (31.18 dB). (e) LGSR (31.34 dB).

image restoration methods exploit the strong correlation of nonlocal similar patches to preserve image texture information effectively [4], [17], [24], [26]. However, they have imposed only plain sparsity over the individual patch of the group in image modeling, and the restoration results are limited by ignoring other beneficial image properties. Since all the patches (each patch is unfolded into a vector) in each group have similar patterns, the constructed group matrix has the LR property [27], [28]. The LR model [6], [8], [9], [29]–[33], i.e., each patch group lives in a low-dimensional subspace [34], [35], has also been shown effective in many image restoration tasks [3], [8], [9]. For example, Zhang *et al.* [3] proposed an LR-based dictionary learning approach for image restoration. Gu *et al.* [8] proposed an effective nonlocal-based image denoising algorithm by enforcing the weighted nuclear norm minimization (WNNM) to the constructed group within many similar patches. Zha *et al.* [9] designed a rank residual constraint (RRC) model from the perspective of approximation theory, which has achieved a better performance than the traditional LR methods for various image restoration tasks. It is worth noting that the constructed group of nonlocal similar patches that are modeled by LR can well restore the structure information of natural images in general [6], [8], [9] but usually tend to be over-smooth due to the truncation of the non-LR components. Fig. 1 shows a widely used image Monarch, which is decomposed into an image with large singular values and an image with small singular values. It is clear that the image with small singular values (non-LR components) also contains important texture information.

Bearing these concerns in mind, in this article, we propose a novel low-rankness guided group sparse representation (LGSR) model and demonstrate its effectiveness in many image restoration tasks, including denoising, inpainting, and compressive sensing (CS). The proposed LGSR model reconciles the reconstruction estimates based on the group sparsity and LR, which are mutually complementary by preserving the image texture and structure information for high-quality image restoration. Fig. 2 shows an example of image denoising results by comparing our proposed LGSR with the state-of-the-art GSR (i.e., GSRC-NLP [17]) and LR (i.e., WNNM [22]) methods. We can see that the proposed LGSR is able to recover finer image details than other competing methods. The main contributions of this article are summarized as follows.

1) We propose a novel LGSR model that jointly exploits the sparsity and LR priors of each group under a unified framework.
2) We develop a simple yet effective algorithm to solve the proposed LGSR-based image restoration problem by alternating minimization. Moreover, some strategies to adaptively adjust parameters are provided in the optimization.

The remainder of this article is organized as follows. Section II introduces some related works for image restoration. Section III presents some preliminaries, including the GSR and LR approximation models. Section IV presents the proposed LGSR model and explores its applications to image restoration. Section V uses an alternating minimization method with an adaptively adjusted parameter scheme to solve the optimization problem. The experimental results are presented in Section VI, and Section VII provides several concluding remarks.

II. Related Works

In the processing of image formulation, degradation (e.g., noise, blurry, pixel missing, and down-sampling) inevitably exists in many digital imaging devices, which leads to the acquired image being diverged from the unknown latent clean image. Therefore, reconstructing the latent high-quality image from its degraded observation has increasingly attracted more interest in recent years. Image restoration is an ill-posed inverse problem in nature [36]. To cope with this, image prior knowledge is widely applied to improve the quality of the reconstructed images. Therefore, employing image prior to design the effective regularization models plays an essential role in image restoration [1]–[4], [8], [9], [15], [36], [37], [37], [38].

Early image priors mainly focus on exploiting the local correlation of image pixels. A well-known regularization model, termed total variation (TV) [1], assumes that the image gradient can be modeled as a Laplacian distribution. Most TV-based image restoration methods can effectively remove noise artifacts but are apt to over-smooth the images. Thus, they usually result in missing fine details. Alternatively, it is well known that natural images can be modeled by the patch prior [2]. The representative one is the sparse representation model [2], [14], which signifies that each patch as a sparse

coefficient in which most of the elements are zeros through the learned dictionaries [3], [14], [19], while others have proposed adaptive sparsity in the transform domains [7], [20]. Nonetheless, most patch-based sparse representation models have only considered the local image structures while neglecting the strong correlation among similar patches, such as the image NSS property [15], [17], [19], [24].

Combining image NSS with sparsity priors, GSR models utilize each group (including many nonlocal similar patches) as the basic unit of sparse representation, which have achieved an excellent performance in numerous image restoration applications [3], [17], [19], [26], [39]. For instance, BM3D [39] first utilized both image NSS and sparsity priors for image denoising, which remains an image denoising benchmark method. The LSSC model [19] enforced that all sparse coefficients in each group share the same support. Zhang *et al.* [3] designed an adaptive dictionary under the framework of GSR for image restoration. Xu *et al.* [26] proposed a GSR model with learning an external NSS prior to image denoising. Zha *et al.* [17] designed an effective GSR model with a structural residual constraint for image restoration, which has attained a state-of-the-art performance. Another representative method is the LR approximation [6], [8], [9], which exploits the LR property of the constructed group matrix. Some LR approximation methods (e.g., SAIST [6], WNNM [8], and RRC [9]) have also been verified to be effective for various image restoration tasks.

Most recently, deep convolutional neural networks (CNNs) have been proven as a powerful tool for image restoration [10], [11], [24], [40]–[43]. For example, the most representative work is the SRCNN [24] for image super-resolution, which learns two hidden layers directly to map low-/high-resolution images. Zhang *et al.* [40] designed an end-to-end trainable deep CNN framework for image restoration, which employs the residual learning strategy to estimate the restored image from degraded observation. Dong *et al.* [41] learned a denoiser prior-driven deep CNN for image restoration, which utilizes both the optimization and discriminative learning techniques. Shi *et al.* [42] devised an image CS method based on CNN, which jointly optimizes the sampling network and the reconstructed network. Nevertheless, most of the existing deep CNN-based image restoration methods merely focus on considering the local properties of images while do not explicitly use image NSS prior [44], which may limit their performance. Therefore, in order to ameliorate this shortcoming, the self-attention mechanism of CNN is considered to exploit NSS for image restoration [45]–[48]. For instance, Liu *et al.* [45] designed a nonlocal recurrent network for image restoration. Zhang *et al.* [36] proposed a residual nonlocal attention network for image restoration.

III. Preliminaries

In this section, we briefly introduce the GSR model [3], [4], [17] and the LR approximation model [6], [8], [9].

A. Group Sparse Representation

GSR is usually a two-stage strategy: patch grouping for depicting the self-similarity of an image, followed by sparsity enforcement for each group of similar patches [3], [4], [17]. Specifically, given an image $\boldsymbol{x} \in \mathbb{R}^N$, it is divided into n overlapped patches $\boldsymbol{x}_i$ of size $\sqrt{b} \times \sqrt{b}$. Then, for each exemplar patch $\boldsymbol{x}_i$, we perform a variant of the k-nearest-neighbor (KNN) algorithm [49]–[51] within a local window $L \times L$ to search m most similar patches. After this, the selected m similar patches are making up a group matrix $\boldsymbol{X}_i \in \mathbb{R}^{b\times m}$, i.e., $\boldsymbol{X}_i = \{\boldsymbol{x}_{i,1}, \boldsymbol{x}_{i,2}, \ldots, \boldsymbol{x}_{i,m}\}$, where each column $\boldsymbol{x}_{i,j}$ in $\boldsymbol{X}_i$ denotes the j-th patch similar to the exemplar patch $\boldsymbol{x}_i$ $\forall j = 1, \ldots, m$. The matrix $\boldsymbol{X}_i$ consisting of patches with similar structures is thereby called a group. In general, the GSR model learns a dictionary $\boldsymbol{D}_i$ from each group $\boldsymbol{X}_i$ [3], [4], [26]. Considering the learned dictionary $\boldsymbol{D}_i$, each group $\boldsymbol{X}_i$ can be sparsely represented by solving the following minimization problem [4]:

$$\hat{\boldsymbol{A}}_i = \arg\min_{\boldsymbol{A}_i} \left(\frac{1}{2} \|\boldsymbol{X}_i - \boldsymbol{D}_i \boldsymbol{A}_i\|_F^2 + \lambda \|\boldsymbol{A}_i\|_1 \right) \quad \forall i \tag{1}$$

where the notation $\| \ \|_F$ denotes the Frobenius norm, and $\|\cdot\|_1$ denotes the ℓ_1-norm, which is imposed on each column in $\boldsymbol{A}_i$, and here it is extended to be the ℓ_1-norm on matrix. λ is a nonnegative constant. Once all group sparse coefficients $\{\hat{\boldsymbol{A}}_i\}_{i=1}^n$ are attained by solving (1), the underlying desired image $\hat{\boldsymbol{x}}$ can be reconstructed by $\hat{\boldsymbol{x}} = \boldsymbol{D}\hat{\boldsymbol{A}}$, where $\boldsymbol{D}$ and $\hat{\boldsymbol{A}}$ represent a set of $\{\boldsymbol{D}_i\}_{i=1}^n$ and $\{\hat{\boldsymbol{A}}_i\}_{i=1}^n$, respectively.

B. LR Approximation

Based on the group construction procedure in Section III-A, the constructed group matrix $\boldsymbol{X}_i$ within many nonlocal similar patches has the LR property [27], [28]. Inspired by this crucial property, the LR approximation methods have been widely used for a variety of image restoration applications [6], [8], [9]. The most representative work is nuclear norm minimization (NNM) [6]. Specifically, given a matrix $\boldsymbol{X}_i \in \mathbb{R}^{b\times m}$, the goal of NNM is to achieve an LR matrix $\boldsymbol{Z}_i$ of rank $r \ll \min(\mathrm{b}, \mathrm{m})$, which is formulated as follows:

$$\hat{\boldsymbol{Z}}_i = \arg\min_{\boldsymbol{Z}_i} \left(\frac{1}{2} \|\boldsymbol{X}_i - \boldsymbol{Z}_i\|_F^2 + \lambda \|\boldsymbol{Z}_i\|_* \right) \quad \forall i \tag{2}$$

where $\| \ \|_*$ represents the nuclear norm [52]. The underlying desired image $\hat{\boldsymbol{x}}$ can be reconstructed by aggregating all the LR matrices $\{\hat{\boldsymbol{Z}}_i\}_{i=1}^n$. In recent years, some advanced LR approximation methods are developed to improve the accuracy of rank estimation, such as WNNM [8] and RRC [9], which have achieved an excellent performance for various image restoration tasks.

IV. Proposed Method

In this section, we propose the LGSR model, which jointly investigates the group sparsity and LR properties of natural images. Furthermore, we apply the proposed LGSR model to image restoration.

A. Low-Rankness Guided Group Sparse Representation

As mentioned earlier, most of the existing GSR models exploit the strong correlation of similar nonlocal patches to preserve image texture information effectively [4], [19], [26]. However, they have imposed only plain sparsity over the

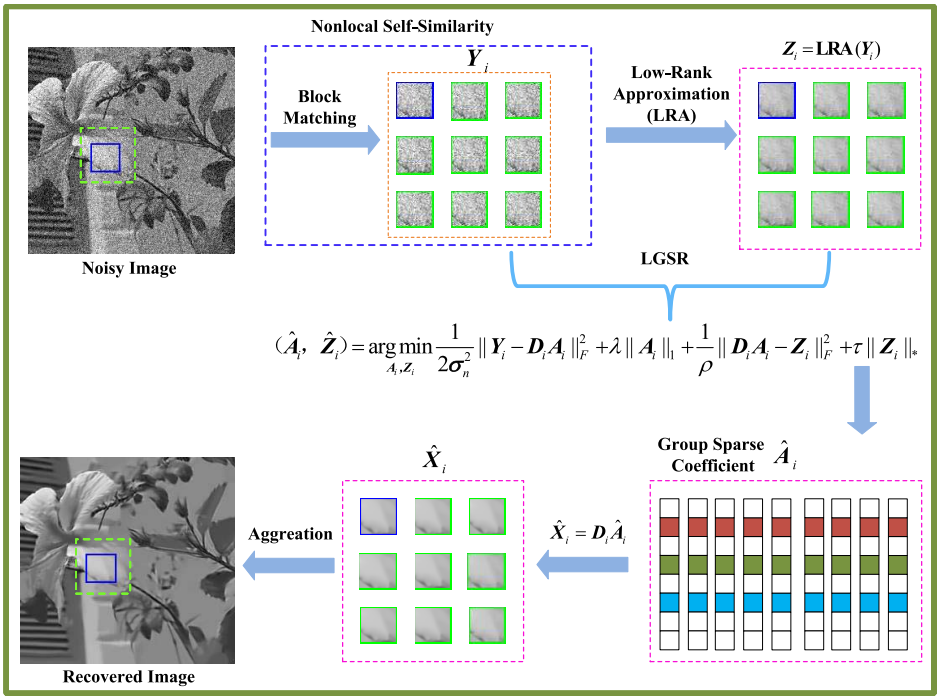

Fig. 3. Flowchart of the proposed LGSR for image denoising. The noisy image is reconstructed using our proposed LGSR model by jointly employing group sparsity with LR priors under a unified framework.

individual patch of the group in image modeling, and the restoration results are limited by neglecting other beneficial image properties. To further mine the intrinsic property of natural images, the dual regularizers are employed in our proposed model, i.e., the group sparsity and LR penalties. This leads to the following LGSR problem:

$$\{\hat{\boldsymbol{A}}_i, \hat{\boldsymbol{Z}}_i\} = \arg\min_{\boldsymbol{A}_i, \boldsymbol{Z}_i} \frac{1}{2}\|\boldsymbol{X}_i - \boldsymbol{D}_i\boldsymbol{A}_i\|_F^2 + \lambda\|\boldsymbol{A}_i\|_1 + \frac{1}{\rho}\|\boldsymbol{D}_i\boldsymbol{A}_i - \boldsymbol{Z}_i\|_F^2 + \tau\|\boldsymbol{Z}_i\|_* \quad \forall i \tag{3}$$

where $\|\ \|_1$ and $\|\ \|_*$ are employed to impose the group sparsity penalty and the LR penalty, respectively. ρ is a balance factor to make the solution of (3) more feasible, and τ is a regularization parameter. Apparently, unlike the conventional GSR models [4], [17], [24], [26], [39], in the proposed LGSR model, the LR approximation $\boldsymbol{Z}_i$ is jointly estimated for each reconstructed group $\boldsymbol{D}_i\boldsymbol{A}_i$, which not only further explores the LR property of each group but also serves as the complementary priors for preserving the texture and structure information of natural images. Finally, similar to GSR in (1), the optimal group sparse codes $\{\hat{\boldsymbol{A}}_i\}_{i=1}^n$ are employed to reconstruct the latent desired image. We use image denoising as an example, and the flowchart of the proposed LGSR for image denoising is illustrated in Fig 3.

Note that the LR property of the group coefficient is employed in the LR-GSC method [53], which may lead to a suboptimal solution, because each group coefficient cannot guarantee that it has an LR property. Compared with the LR-GSC method, the LR property of each reconstructed group is explicitly employed to improve the accuracy of the group sparse codes in our proposed LGSR model (3). In the experiments, we demonstrate that the proposed LGSR is more effective than the LR-GSC method [53] (see Section VI-D for more details).

B. LGSR for Image Restoration

The goal of image restoration is to restore the high-quality image $\boldsymbol{x}$ from its degraded observation $\boldsymbol{y}$, which can be mathematically modeled as

$$\boldsymbol{y} = \boldsymbol{H}\boldsymbol{x} + \boldsymbol{n} \tag{4}$$

where $\boldsymbol{H}$ is the degradation operator relating to an imaging system, and $\boldsymbol{n}$ is usually assumed to be additive Gaussian white noise with variance $\boldsymbol{\sigma}_n^2$. Specifying different degradation operators $\boldsymbol{H}$ corresponds to different image restoration problems. For instance, (4) reduces to a simple image denoising problem [22], [39] when $\boldsymbol{H}$ is an identity matrix; (4) becomes an image deblurring problem [3], [10] when $\boldsymbol{H}$ is a convolution operator; (4) becomes an image inpainting problem [4], [6] when $\boldsymbol{H}$ is a diagonal masking matrix; and (4) represents an image CS problem [53], [54] when $\boldsymbol{H}$ is a random projection matrix.

Due to the ill-posed nature of the image restoration problem (4), a common practice is to employ regularization techniques to adjust the solution spaces. In order to design a high-effective regularizer for image restoration, it is critical to exploit the prior information of the original image $\boldsymbol{x}$. Therefore, based on certain image priors of the original image $\boldsymbol{x}$, the regularization-based models for image restoration are usually represented as [4], [23]

$$\hat{\boldsymbol{x}} = \arg\min_{\boldsymbol{x}} \frac{1}{2\boldsymbol{\sigma}_n^2}\|\boldsymbol{y} - \boldsymbol{H}\boldsymbol{x}\|_2^2 + \lambda\Phi(\boldsymbol{x}) \tag{5}$$

where the first term denotes the data fidelity, and $\|\cdot\|_2$ represents the ℓ_2-norm. The second term is the regularizer based on the prior knowledge of image $\boldsymbol{x}$, and λ represents the regularization parameter.

In this section, we employ the proposed LGSR model for image restoration. More specifically, the proposed LGSR prior model (3) is integrated into the regularization-based framework of (5), and then, the proposed LGSR-based image restoration is expressed as

$$\begin{aligned}\left(\hat{\boldsymbol{x}}, \{\hat{\boldsymbol{A}}_i\}_{i=1}^n, \{\hat{\boldsymbol{Z}}_i\}_{i=1}^n\right) = \arg\min_{\boldsymbol{x},\boldsymbol{A}_i,\boldsymbol{Z}_i} & \frac{1}{2\boldsymbol{\sigma}_n^2}\|\boldsymbol{y}-\boldsymbol{H}\boldsymbol{x}\|_2^2 \\ & + \frac{1}{2\mu}\sum_{i=1}^n \|\boldsymbol{R}_i\boldsymbol{x}-\boldsymbol{D}_i\boldsymbol{A}_i\|_F^2 + \lambda\sum_{i=1}^n \|\boldsymbol{A}_i\|_1 \\ & + \frac{1}{2\rho}\sum_{i=1}^n \|\boldsymbol{D}_i\boldsymbol{A}_i-\boldsymbol{Z}_i\|_F^2 + \tau\sum_{i=1}^n \|\boldsymbol{Z}_i\|_*\end{aligned} \tag{6}$$

where $\boldsymbol{R}_i$ denotes a KNN operator [8], [39] that picks up the group $\boldsymbol{X}_i$ from the image $\boldsymbol{x}$, namely, $\boldsymbol{R}_i\boldsymbol{x} = [\boldsymbol{x}_{i,1}, \ldots, \boldsymbol{x}_{i,m}] \in \mathbb{R}^{b\times m}$ represents the group matrix $\boldsymbol{X}_i$ formed by m closest patches for each exemplar patch $\boldsymbol{x}_i$. μ has the same role as ρ. It is clearly seen that the proposed LGSR-based image restoration model (6) not only jointly utilizes the group sparsity and LR properties of each group but also plays a mutually complementary role in preserving the image texture and structure information. Therefore, our proposed LGSR-based image restoration algorithm can achieve better restoration results than some existing methods based on a single prior (see Section VI for more details). In the following, we describe how to solve the proposed LGSR-based image restoration problem (6).

V. Optimization for the LGSR Problem

In this section, an alternating minimization method [55]–[57] is employed to solve the proposed LGSR-based image restoration problem (6) concerning three subproblems, i.e., $\boldsymbol{A}_i$, $\boldsymbol{Z}_i$, and $\boldsymbol{x}$ subproblems. Moreover, we present an adaptively adjusted strategy to make the optimization more robust and practical.

A. $\boldsymbol{A}_i$ Subproblem

For fixed $\boldsymbol{Z}_i$ and $\boldsymbol{x}$ and given $\boldsymbol{D}_i$, $\boldsymbol{A}_i$ subproblem in (6) can be reduced to the following problem:

$$\begin{aligned}\{\hat{\boldsymbol{A}}_i\}_{i=1}^n &= \arg\min_{\boldsymbol{A}_i} \frac{1}{2\mu}\sum_{i=1}^n \|\boldsymbol{R}_i\boldsymbol{x}-\boldsymbol{D}_i\boldsymbol{A}_i\|_F^2 \\ &\quad + \frac{1}{2\rho}\sum_{i=1}^n \|\boldsymbol{D}_i\boldsymbol{A}_i-\boldsymbol{Z}_i\|_F^2 + \lambda\sum_{i=1}^n \|\boldsymbol{A}_i\|_1 \\ &= \arg\min_{\boldsymbol{A}_i} \sum_{i=1}^n \left(\frac{1}{2}\|\boldsymbol{G}_i-\boldsymbol{D}_i\boldsymbol{A}_i\|_F^2 + \lambda\mu\rho\|\boldsymbol{A}_i\|_1\right)\end{aligned} \tag{7}$$

where $\boldsymbol{G}_i \triangleq (\rho\boldsymbol{R}_i\boldsymbol{x} + \mu\boldsymbol{Z}_i)/(\rho+\mu)$. It can be seen that how to devise an effective dictionary $\boldsymbol{D}_i$ is a crucial procedure for solving $\boldsymbol{A}_i$ subproblem. Generally speaking, the dictionaries are over-complete, which should satisfy very redundant properties representing diverse image local structures. However, learning an over-complete dictionary is unstable for image restoration, because it is easy to produce visual artifacts [58]. In this section, in order to better adapt to image local structures, we learn a principal component analysis (PCA) subdictionary $\boldsymbol{D}_i$ from each group $\boldsymbol{G}_i$ [59]. Because the learned PCA dictionaries are unitary, then (7) can be equally solved by

$$\{\hat{\boldsymbol{A}}_i\}_{i=1}^n = \arg\min_{\boldsymbol{A}_i} \sum_{i=1}^n \left(\frac{1}{2}\|\boldsymbol{P}_i-\boldsymbol{A}_i\|_F^2 + \lambda\mu\rho\|\boldsymbol{A}_i\|_1\right) \tag{8}$$

where $\boldsymbol{P}_i = \boldsymbol{D}_i^T\boldsymbol{G}_i$. It can be seen that $\boldsymbol{A}_i$ subproblem is now simplified to solve (8). Fortunately, we can obtain a closed-form solution for each $\boldsymbol{A}_i$, namely

$$\hat{\boldsymbol{A}}_i = \text{Soft}(\boldsymbol{P}_i, \lambda\mu\rho) \quad \forall i \tag{9}$$

where $\text{Soft}(\cdot)$ represents the soft-thresholding operator [60], namely, $\text{Soft}(\boldsymbol{P}, \lambda\mu\rho) \triangleq \max(\boldsymbol{P}_{j,k} - \lambda\mu\rho, 0)$, where $\boldsymbol{P}_{j,k}$ denotes the elements of arbitrary matrix $\boldsymbol{P}$.

B. $\boldsymbol{Z}_i$ Subproblem

For fixed $\boldsymbol{A}_i$ and given $\boldsymbol{D}_i$, $\boldsymbol{Z}_i$ subproblem in (6) becomes

$$\{\hat{\boldsymbol{Z}}_i\}_{i=1}^n = \arg\min_{\boldsymbol{Z}_i} \sum_{i=1}^n \left(\frac{1}{2}\|\boldsymbol{D}_i\boldsymbol{A}_i-\boldsymbol{Z}_i\|_F^2 + \rho\tau\|\boldsymbol{Z}_i\|_*\right) \tag{10}$$

where $\|\boldsymbol{Z}_i\|_* = \sum_j \delta_{i,j}\ \forall j = 1, \ldots, d$ and $\delta_{i,j}$ is the j-th singular value of matrix $\boldsymbol{Z}_i$. Based on the singular value thresholding (SVT) algorithm [52], we can obtain a closed-form solution of (10) as follows:

$$\hat{\boldsymbol{Z}}_i = \boldsymbol{U}_i\text{Soft}(\boldsymbol{\Delta}_i, \rho\tau)\boldsymbol{V}_i^T \quad \forall i \tag{11}$$

where $\boldsymbol{D}_i\boldsymbol{A}_i = \boldsymbol{U}_i\boldsymbol{\Delta}_i{\boldsymbol{V}_i}^T$ represents the singular value decomposition (SVD) of the reconstructed group $\boldsymbol{D}_i\boldsymbol{A}_i$ among group sparsity, and the soft-thresholding is enforced to the diagonal elements of the singular value matrix $\boldsymbol{\Delta}_i$.

C. $\boldsymbol{x}$ Subproblem

For fixed $\boldsymbol{A}_i$ and given $\boldsymbol{D}_i$, $\boldsymbol{x}$ subproblem in (6) becomes

$$\hat{\boldsymbol{x}} = \arg\min_{\boldsymbol{x}} \frac{1}{2\boldsymbol{\sigma}_n^2}\|\boldsymbol{y}-\boldsymbol{H}\boldsymbol{x}\|_2^2 + \frac{1}{2\mu}\sum_{i=1}^n \|\boldsymbol{R}_i\boldsymbol{x}-\boldsymbol{D}_i\boldsymbol{A}_i\|_F^2. \tag{12}$$

Apparently, (12) has a closed-form solution, because it is a quadratic minimization problem. In this section, in order to accelerate the optimization, a much faster algorithm is developed to solve (12) via an alternating direction method of multipliers (ADMM) [61] technique. Specifically, we introduce an auxiliary variable $\boldsymbol{s}$ and define $\boldsymbol{x} = \boldsymbol{s}$; in this manner, (12) can be transformed into the following constrained form:

$$\begin{aligned}(\hat{\boldsymbol{x}}, \hat{\boldsymbol{s}}) = \arg\min_{\boldsymbol{x},\boldsymbol{s}} & \frac{1}{2\boldsymbol{\sigma}_n^2}\|\boldsymbol{y}-\boldsymbol{H}\boldsymbol{x}\|_2^2 + \frac{1}{2\mu}\sum_{i=1}^n \|\boldsymbol{R}_i\boldsymbol{s}-\boldsymbol{D}_i\boldsymbol{A}_i\|_F^2 \\ & \text{s.t. } \boldsymbol{s} = \boldsymbol{x}.\end{aligned} \tag{13}$$

By invoking the ADMM algorithm, the minimization of (13) is now transformed into three iterative steps

$$\hat{\boldsymbol{x}}^{t+1} = \arg\min_{\boldsymbol{x}} \frac{1}{2\boldsymbol{\sigma}_n^2}\|\boldsymbol{y}-\boldsymbol{H}\boldsymbol{x}\|_2^2 + \frac{1}{2\gamma}\left\|\boldsymbol{x}-\boldsymbol{s}^t-\boldsymbol{c}^t\right\|_2^2 \quad (14)$$

$$\hat{\boldsymbol{s}}^{t+1} = \arg\min_{\boldsymbol{s}} \frac{1}{2\mu}\sum_{i=1}^{n}\|\boldsymbol{R}_i\boldsymbol{s}-\boldsymbol{D}_i\boldsymbol{A}_i\|_F^2 + \frac{1}{2\gamma}\left\|\boldsymbol{x}^{t+1}-\boldsymbol{s}-\boldsymbol{c}^t\right\|_2^2 \quad (15)$$

$$\hat{\boldsymbol{c}}^{t+1} = \boldsymbol{c}^t - \left(\boldsymbol{x}^{t+1}-\boldsymbol{s}^{t+1}\right) \quad (16)$$

where t denotes the t-th iteration, and $\boldsymbol{c}$ represents the Lagrangian multiplier. One can observe that the minimization for (13) involves two subproblems, namely, $\boldsymbol{x}$ and $\boldsymbol{s}$ subproblems. Fortunately, there is an efficient solution to each subproblem, which will be introduced later. To be simple and without confusion, we will omit the subscript t for conciseness.

1) Solution of $\boldsymbol{s}$ Subproblem: For fixed $\boldsymbol{D}_i\boldsymbol{A}_i$, $\boldsymbol{x}$, and $\boldsymbol{c}$, $\boldsymbol{s}$ admits a closed-form solution, that is

$$\hat{\boldsymbol{s}} = \left(\gamma\sum_{i=1}^{n}\boldsymbol{R}_i^T\boldsymbol{R}_i + \mu\boldsymbol{I}\right)^{-1}\left(\mu\boldsymbol{x}-\mu\boldsymbol{c}+\gamma\sum_{i=1}^{n}\boldsymbol{R}_i^T\boldsymbol{D}_i\boldsymbol{A}_i\right) \quad (17)$$

where $\boldsymbol{I}$ denotes an identity matrix, $\boldsymbol{R}_i^T\boldsymbol{R}_i = \Sigma_{j=1}^{m}\boldsymbol{R}_{i,j}^T\boldsymbol{R}_{i,j}$, and $\boldsymbol{R}_i^T\boldsymbol{D}_i\boldsymbol{A}_i = \Sigma_{j=1}^{m}\boldsymbol{R}_{i,j}^T\boldsymbol{D}_{i,j}\boldsymbol{A}_{i,j}$. Note that (17) can be efficiently solved by an elementwise division, as $(\gamma\sum_{i=1}^{n}\boldsymbol{R}_i^T\boldsymbol{R}_i+\mu\boldsymbol{I})$ is essentially a diagonal matrix.

2) Solution of $\boldsymbol{x}$ Subproblem: For fixed $\boldsymbol{s}$ and $\boldsymbol{c}$, the variable $\boldsymbol{x}$ also has a closed-form solution, namely

$$\hat{\boldsymbol{x}} = \left(\gamma\boldsymbol{H}^T\boldsymbol{H}+\boldsymbol{\sigma}_n^2\boldsymbol{I}\right)^{-1}\left(\gamma\boldsymbol{H}^T\boldsymbol{y}+\boldsymbol{\sigma}_n^2\boldsymbol{s}+\boldsymbol{\sigma}_n^2\boldsymbol{c}\right). \quad (18)$$

However, in image CS, $\boldsymbol{H}$ is a random projection matrix with no specific structure, which usually needs a high computational cost due to computing matrix inverse. As a result, in order to avert calculating the matrix inverse, we employ a gradient descent method [62] to solve (14) for the image CS task, namely

$$\hat{\boldsymbol{x}} = \boldsymbol{x}-\eta\boldsymbol{q} \quad (19)$$

where $\boldsymbol{q}$ denotes the gradient direction of (14), and η is the step size. In this manner, we only require an iterative calculation to solve the $\boldsymbol{x}$ subproblem, namely

$$\hat{\boldsymbol{x}} = \boldsymbol{x}-\eta\left(\frac{1}{\boldsymbol{\sigma}_n^2}(\boldsymbol{H}^T\boldsymbol{H}\boldsymbol{x}-\boldsymbol{H}^T\boldsymbol{y})+\frac{1}{\gamma}(\boldsymbol{x}-\boldsymbol{s}-\boldsymbol{c})\right) \quad (20)$$

where $\boldsymbol{H}^T\boldsymbol{H}$ and $\boldsymbol{H}^T\boldsymbol{y}$ can be calculated in advance to make the aforementioned computation efficient.

D. Adaptively Adjusted Parameters

We can see that there are four hyperparameters in the proposed LGSR-based image restoration model (6), i.e., μ, ρ, λ, and τ. We usually empirically choose the fixed values for these parameters. Nevertheless, in this way, it cannot assure the stability of the whole algorithm. Therefore, we present an adaptively adjusted parameter strategy to make the proposed algorithm more robust and practical. Expressly, we set the balance factors μ and ρ of the quadratic term to be proportional to the noise variance $\boldsymbol{\sigma}_e^2$ in each iteration, that is

$$\mu^{(t)} = \alpha\ \left(\boldsymbol{\sigma}_e^2\right)^{(t)}, \quad \rho^{(t)} = \beta\ \left(\boldsymbol{\sigma}_e^2\right)^{(t)} \quad (21)$$

where α and β represent the scaling factors. We can see that the balance factors μ and ρ depend on the estimation of noise variance $\boldsymbol{\sigma}_e^2$. In this article, the iterative regularization strategy [1] is used for updating $\boldsymbol{\sigma}_e^{(t)}$

$$\boldsymbol{\sigma}_e^{(t)} = \omega\sqrt{\boldsymbol{\sigma}_n^2-\|\hat{\boldsymbol{x}}^{(t)}-\boldsymbol{y}\|_2^2} \quad (22)$$

where ω denotes a scaling factor. This iterative regularization strategy has been widely used in image denoising with the Gaussian noise removal [8], [9], [26].

Besides, in each iteration, the regularization parameters λ and τ are adaptively adjusted for the sparsity and LR penalties, respectively, by [6]

$$\lambda^{(t)} = \frac{2\sqrt{2}\left(\boldsymbol{\sigma}_e^{(t)}\right)^2}{(\boldsymbol{\alpha}_i+\varepsilon)}, \quad \tau^{(t)} = \frac{2\sqrt{2}\left(\boldsymbol{\sigma}_e^{(t)}\right)^2}{\left(\boldsymbol{\beta}_i+\epsilon\right)} \quad (23)$$

Algorithm 1 Image Restoration by LGSR

Require: The degraded image $\boldsymbol{y}$ and the measurement matrix $\boldsymbol{H}$.
Initialization: $\hat{\boldsymbol{x}}^0 = \boldsymbol{y}$ and parameters b, m, W, α, β, γ and ω.
for $t = 1$ **to** Max-Iter **do**
  Compute $\boldsymbol{\sigma}_e$ via (22).
  $\boldsymbol{x}^{(t)}$ is divided into a set of overlapping patches with size $\sqrt{b}\times\sqrt{b}$;
  for Each patch $\boldsymbol{x}_i$ in $\boldsymbol{x}^t$ **do**
    Discover nonlocal similar patches to generate a group $\boldsymbol{X}_i$ and let $\boldsymbol{D}_i\boldsymbol{A}_i = \boldsymbol{X}_i$.
  end for
  for Each group $\boldsymbol{X}_i$ in $\boldsymbol{x}^t$ **do**
    Perform $[\boldsymbol{U}_i, \boldsymbol{\Delta}_i, \boldsymbol{V}_i] = \mathrm{SVD}(\boldsymbol{D}_i\boldsymbol{A}_i)$;
    Compute β via (21);
    Compute τ via (23);
    Compute $\hat{\boldsymbol{Z}}_i$ via (11);
    Constructing dictionary $\boldsymbol{D}_i$ by $\boldsymbol{G}_i$ using PCA;
    Compute α via (21);
    Compute λ via (23);
    Compute $\hat{\boldsymbol{A}}_i$ via (9);
  end for
  ADMM:
  Initialization: $\boldsymbol{c} = 0$ and $\boldsymbol{s} = \hat{\boldsymbol{x}}^{(t)}$.
  if $\boldsymbol{H}$ is not random projection operator **then**
    Compute $\boldsymbol{x}^{(t+1)}$ via (18);
  else
    Compute $\boldsymbol{x}^{(t+1)}$ via (20);
  end if
  Compute $\boldsymbol{s}^{(t+1)}$ via (17);
  Compute $\boldsymbol{c}^{(t+1)}$ via (16);
end for
Output: The final restored image $\hat{\boldsymbol{x}} = \boldsymbol{x}^{(t+1)}$.

TABLE I

AVERAGE PSNR (dB) AND SSIM COMPARISON RESULTS WITH DIFFERENT NOISE LEVELS ON TESTING THE BSD200 DATASET [63] VIA DIFFERENT IMAGE DENOISING METHODS

σ_n	BM3D [39]	LSSC [19]	EPLL [64]	NCSR [14]	PGPD [26]	OGLR [65]	RRC [9]	GSRC-NLP [17]	WNNM [22]	LGSR
20	29.86	30.02	29.96	29.89	29.89	29.67	29.98	29.90	30.11	30.11
	0.8476	0.8520	0.8528	0.8449	0.8393	0.8448	0.8518	0.8397	0.8481	**0.8533**
30	27.93	28.05	28.00	27.92	27.96	27.84	28.02	27.91	28.17	28.15
	0.7875	0.7936	0.7902	0.7861	0.7803	0.7852	0.7926	0.7758	0.7905	**0.7956**
40	26.58	26.75	26.71	26.58	26.73	26.65	26.73	26.68	26.88	26.87
	0.7387	0.7459	0.7387	0.7337	0.7359	0.7444	0.7471	0.7351	0.7412	**0.7478**
50	25.71	25.80	25.77	25.65	25.82	25.69	25.81	25.73	25.96	25.94
	0.7041	0.7068	0.6963	0.6976	0.6986	0.7000	0.7108	0.6939	0.7089	**0.7120**
75	24.22	24.18	24.18	24.04	24.30	24.16	24.28	24.17	24.42	24.38
	0.6337	0.6364	0.6160	0.6320	0.6330	0.6234	0.6433	0.6336	0.6446	**0.6452**
100	23.21	23.12	23.15	23.00	23.29	22.85	23.27	23.02	23.37	23.34
	0.5814	0.5873	0.5566	0.5889	0.5810	0.5528	0.5986	0.5882	0.5949	**0.6040**
Average	26.25	26.32	26.30	26.18	26.33	26.14	26.35	26.24	26.49	26.47
	0.7155	0.7203	0.7084	0.7139	0.7114	0.7084	0.7240	0.7111	0.7214	**0.7263**

Fig. 4. Some test images for the experiments. Top row: Cowboy, Bear, House, Lake, Leaves, and Lena. Bottom row: Lily, Flowers, Nanna, Agaric, Fireman, and Girls.

where $\boldsymbol{\alpha}_i$ and $\boldsymbol{\beta}_i$ are the estimated standard variance of $\hat{\boldsymbol{A}}_i$ and $\hat{\boldsymbol{\Delta}}_i$, respectively. ε and ϵ represent small constants to avoid dividing by zero.

Until now, we have introduced an adaptively adjusted parameter strategy in the proposed LGSR-based image restoration model to solve the aforementioned three subproblems, i.e., $\boldsymbol{A}_i$, $\boldsymbol{Z}_i$, and $\boldsymbol{x}$. We can achieve an efficient solution by solving each subproblem individually, bringing about the entire algorithm more stable and practical. We summarize the complete procedure of the proposed LGSR for image restoration in Algorithm 1.

VI. EXPERIMENTAL RESULTS

In this section, we conduct extensive experiments to illustrate the effectiveness of the proposed LGSR-based image restoration algorithm. Three classic image restoration tasks are considered, including denoising, inpainting, and CS. We jointly utilize the peak signal-to-noise ratio (PSNR) and structural similarity (SSIM) [66] as evaluation metrics for restoration results. Some test images are presented in Fig. 4. Because human visual perception is sensitive to luminance changes in color images, in this article, we only focus on the restoration of the luminance component for color images. The restoration results of all competing methods are attained by performing the codes with the default parameter settings derived from the original authors. The source code of our proposed LGSR model for image restoration is available at: https://drive.google.com/file/d/10pVoVl1r3virKLLEgcxMwRZ3F2JiGqw2/view?usp=sharing.

A. Image Denoising

In this section, we apply the proposed LGSR to image denoising. The parameters of the proposed LGSR used for image denoising are set as follows. Similar to [22], the patch size $\sqrt{b} \times \sqrt{b}$ and the nonlocal similar patches m are set to $(6 \times 6, 60)$, $(7 \times 7, 80)$, $(8 \times 8, 100)$, and $(9 \times 9, 120)$ for $\boldsymbol{\sigma}_n \leq 20$, $20 < \boldsymbol{\sigma}_n \leq 40$, $40 < \boldsymbol{\sigma}_n \leq 60$, and $\boldsymbol{\sigma}_n > 60$, respectively. β is set to 0.4 and 0.7 for $\boldsymbol{\sigma}_n \leq 30$ and $\boldsymbol{\sigma}_n > 30$, respectively. Moreover, we fix $\omega = 0.3$ for all noise levels.

First, we compare our proposed LGSR with several state-of-the-art classic denoising approaches, including BM3D [39], LSSC [19], EPLL [64], NCSR [14], PGPD [26], OGLR [65], RRC [9], GSRC-NLP [17], and WNNM [22]. Note that the nonlocal redundancies are used in all compared methods. Among them, BM3D, LSSC, EPLL, NCSR, PGPD, OGLR, and GSRC-NLP are the GSR-based image restoration methods. RRC and WNNM are the LR approximation methods, which provide superior results for image denoising. We comprehensively evaluate the denoising performance of all compared methods on testing 200 natural images from the Berkeley Segmentation Dataset (BSD200) [63]. Due to the limited space, we have only presented six noise levels, i.e., $\boldsymbol{\sigma}_n = 20$, 30, 40, 50, 75, and 100. Table I summarizes the average PSNR and SSIM results among all competing methods. As can be seen in Table I, based on the PSNR metric, our proposed LGSR achieves the comparative PSNR results compared with the WNNM method on all noise levels and higher PSNR results than other competing methods. Based on the SSIM metric, our proposed LGSR obtains the highest performance than other competing methods. In particular, our proposed LGSR achieves an SSIM gain over BM3D by 0.0108, over LSSC by 0.0060, over EPLL by 0.0179 dB, over NCSR by 0.0125, over PGPD by 0.0150, over OGLR by 0.0179, over RRC by 0.0023, over GSRC-NLP by 0.0153, and over WNNM by 0.0050. However, we find a fascinating phenomenon: though the PSNR results of the LGSR method are slightly lower than WNNM, the SSIM results of the LGSR method are better than WNNM. As far as we know, the human visual system is considered in SSIM, which leads to more accurate evaluation results [67]. These quantitative

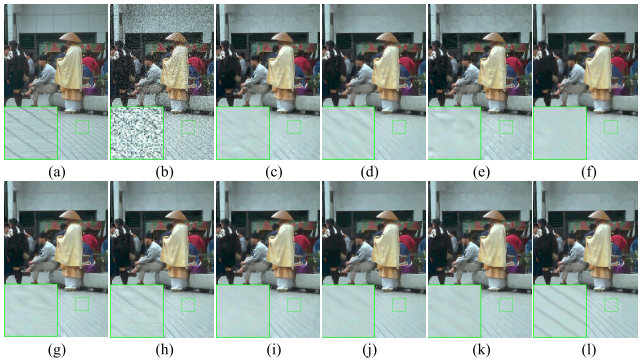

Fig. 5. Denoising results on image 249021 ($\sigma_n = 40$). (a) Original image. (b) Noisy image. (c) BM3D [39] (PSNR = 27.82 dB and SSIM = 0.7212). (d) LSSC [19] (PSNR = 23.29 dB and SSIM = 0.6819). (e) EPLL [64] (PSNR = 27.75 dB and SSIM = 0.8195). (f) NCSR [14] (PSNR = 27.52 dB and SSIM = 0.7008). (g) PGPD [26] (PSNR = 27.96 dB and SSIM = 0.7213). (h) OGLR [65] (PSNR = 27.97 dB and SSIM = 0.7313). (i) RRC [9] (PSNR = 27.93 dB and SSIM = 0.7214). (j) GSRC-NLP [17] (PSNR = 27.93 dB and SSIM = 0.7246). (k) WNNM [22] (PSNR = 27.94 dB and SSIM = 0.7194). (l) LGSR (PSNR = 28.21 dB and SSIM = 0.7475).

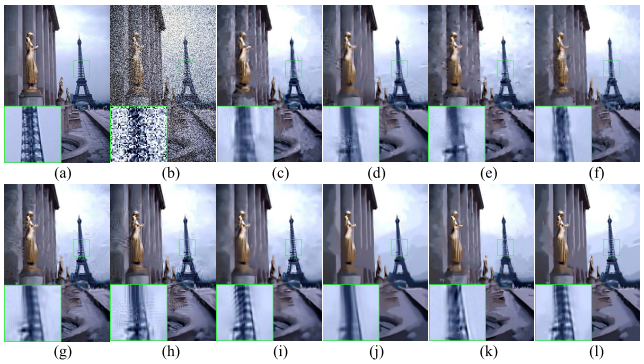

Fig. 6. Denoising results on image 223004 ($\sigma_n = 100$). (a) Original image. (b) Noisy image. (c) BM3D [39] (PSNR = 23.99 dB and SSIM = 0.6614). (d) LSSC [19] (PSNR = 24.01 dB and SSIM = 0.7061). (e) EPLL [64] (PSNR = 23.81 dB and SSIM = 0.6336). (f) NCSR [14] (PSNR = 23.60 dB and SSIM = 0.6865). (g) PGPD [26] (PSNR = 24.17 dB and SSIM = 0.6697). (h) OGLR [65] (PSNR = 23.81 dB and SSIM = 0.6337). (i) RRC [9] (PSNR = 24.32 dB and SSIM = 0.7097). (j) GSRC-NLP [17] (PSNR = 24.27 dB and SSIM = 0.7138). (k) WNNM [22] (PSNR = 24.19 dB and SSIM = 0.6951). (l) LGSR (PSNR = 24.46 dB and SSIM = 0.7153).

results clearly verify the effectiveness of exploiting both the group sparsity and LR properties jointly, as in our proposed LGSR approach.

Human subject perception is the ultimate judge of image quality, which also plays a crucial role in the estimated denoising algorithm. The visual quality comparisons for image 249021 with $\sigma_n = 40$ and image 223004 with $\sigma_n = 100$ are shown in Figs. 5 and 6, respectively. For image 249021, we can see that all compared methods are apt to over-smooth the images. For image 223004, BM3D, EPLL, NCSR, OGLR, and WNNM approaches still suffer from unwished visual artifacts, while LSSC, PGPD, and GSRC-NLP approaches are easy to over-smooth the images and thus lead to some missing details. The RRC method generates better visual comparison results than other competing methods, but it presents a ringing effect. By contrast, the proposed LGSR algorithm not only preserves fine image details but also eliminates the visual artifacts effectively.

TABLE II

AVERAGE PSNR (dB) RESULTS ARE OBTAINED BY OUR PROPOSED LGSR AND THREE DEEP-LEARNING METHODS ON TESTING 12 WIDELY USED IMAGES FROM THE SET12 DATASET [40]

σ_n	TNRD [68]	N2N [69]	S2S [70]	LGSR
15	32.51	32.44	32.09	**32.64**
25	30.06	30.09	30.04	**30.20**
50	26.81	26.96	26.50	**27.00**
Average	29.79	29.83	29.54	**29.95**

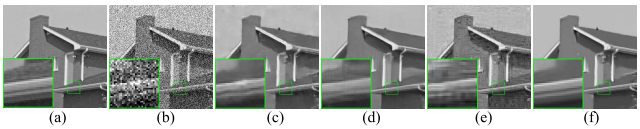

Fig. 7. Denoising results on image 02 ($\sigma_n = 50$). (a) Original image. (b) Noisy image. (c) TNRD [68] (PSNR = 29.49 dB and SSIM = 0.8071). (d) N2N [69] (PSNR = 29.95 dB and SSIM = 0.8156). (e) S2S [70] (PSNR = 27.46 dB and SSIM = 0.6771). (f) LGSR (PSNR = 30.20 dB and SSIM = 0.8274).

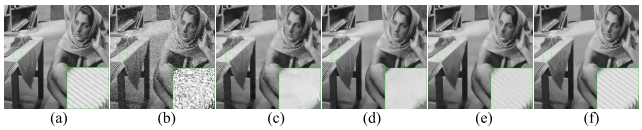

Fig. 8. Denoising results on image 09 ($\sigma_n = 50$). (a) Original image. (b) Noisy image. (c) TNRD [68] (PSNR = 25.70 dB and SSIM = 0.7421). (d) N2N [69] (PSNR = 25.89 dB and SSIM = 0.7536). (e) S2S [70] (PSNR = 27.34 dB and SSIM = 0.7967). (f) LGSR (PSNR = 27.84 dB and SSIM = 0.8265).

To further verify the superiority of the proposed LGSR image denoising algorithm, we now compare it with three deep-learning-based methods, including TNRD [68], N2N [69], and S2S [70]. Note that TNRD and N2N are supervised algorithms, while our proposed LGSR and S2S are self-supervised algorithms. In particular, S2S exploits the strong CNN [71] to train the denoising model from the noisy image itself, which is a state-of-the-art self-supervised deep-learning-based image denoising algorithm. We evaluate the denoising performance of these competing methods on testing the Set12 dataset [40], which is a benchmark dataset for image denoising. We have only provided the comparison results at $\sigma_n = 15$, 25, and 50, because many models in the source code of these competing methods are unavailable. The average PNSR results of these competing methods are shown in Table II, with the best results highlighted in bold. It can be seen that the proposed LGSR achieves the best PSNR results than other competing methods. The average gains of the proposed LGSR over TNRD, N2N, and S2S are as much as 0.15, 0.11, and 0.40 dB, respectively.

Figs. 7 and 8 present the visual comparison results for image 02 and image 09, with $\sigma_n = 50$, respectively. For image 02, it can be seen that TNRD and S2S methods produce agonizing visual artifacts, while the N2N approach tends to over-smooth the image. For image 09, we can see that TNRD and N2N are prone to over-smooth the images, which lose many vital details. Although S2S obtains better visual results than TNRD and N2N approaches, it generates unpleasant visual artifacts. By contrast, the proposed LGSR not only

TABLE III

PSNR (dB) COMPARISON RESULTS OF IMAGE INPAINTING ARE ACHIEVED BY DIFFERENT METHODS ON TESTING 12 NATURAL IMAGES

	80% pixels missing												
Images	**Cowboy**	**Bear**	**House**	**Lake**	**Leaves**	**Lena**	**Lily**	**Flowers**	**Nanna**	**Agaric**	**Girls**	**Fireman**	**Average**
SALSA [72]	23.72	29.42	29.54	24.94	22.03	28.20	26.57	26.81	24.12	27.42	23.79	24.38	25.91
BPFA [73]	24.93	30.04	30.80	25.82	23.78	29.50	27.30	27.30	24.71	27.93	24.80	24.88	26.82
IPPO [74]	25.38	30.08	33.65	25.48	25.56	30.64	28.33	27.70	25.60	29.10	25.31	25.56	27.70
JSM [75]	25.40	29.97	34.31	25.82	26.18	30.46	27.99	27.41	25.33	28.25	25.18	25.31	27.64
GSR [3]	25.35	30.28	35.57	25.68	27.46	31.42	28.86	27.09	25.23	29.47	25.50	25.45	28.11
Aloha [76]	25.06	29.97	33.79	25.32	25.90	30.89	27.70	27.49	25.54	28.63	25.16	25.03	27.54
NGS [77]	24.21	29.83	31.34	25.10	23.87	28.87	27.08	27.03	24.58	27.86	24.27	24.54	26.55
TSLRA [78]	25.36	29.68	32.37	25.47	25.47	30.58	28.17	27.72	25.55	28.85	25.15	25.69	27.50
JPG-SR [79]	25.57	30.13	34.99	25.92	27.36	31.48	28.97	27.46	25.65	29.16	25.61	25.47	28.15
LGSR	**25.65**	**30.55**	**35.83**	**26.33**	**27.48**	**31.69**	**29.07**	**28.03**	**25.91**	**29.61**	**25.81**	**25.79**	**28.48**
	70% pixels missing												
Images	**Cowboy**	**Bear**	**House**	**Lake**	**Leaves**	**Lena**	**Lily**	**Flowers**	**Nanna**	**Agaric**	**Girls**	**Fireman**	**Average**
SALSA [72]	25.70	31.01	31.58	26.76	24.36	28.82	28.35	28.24	25.44	28.69	25.47	25.82	27.52
BPFA [73]	26.76	31.70	33.75	27.93	26.98	31.62	29.30	28.92	26.62	29.65	26.86	26.55	28.89
IPPO [74]	27.40	31.92	36.64	27.56	28.58	32.97	30.28	29.20	27.44	31.14	27.43	27.44	29.83
JSM [75]	27.11	31.59	36.71	27.88	29.28	32.69	29.83	29.06	27.34	30.31	27.20	27.16	29.68
GSR [3]	27.63	32.01	37.62	28.07	31.18	33.54	31.10	29.56	27.89	31.42	27.86	27.48	30.45
Aloha [76]	27.24	31.25	36.68	27.58	29.04	32.80	29.58	29.02	27.43	30.78	27.08	26.52	29.58
NGS [77]	26.19	31.42	33.91	27.01	26.44	30.77	28.83	28.48	26.35	29.49	26.18	26.29	28.45
TSLRA [78]	27.12	31.66	36.15	27.32	28.03	32.64	29.92	29.32	27.32	30.82	27.09	27.22	29.55
JPG-SR [79]	27.51	32.18	37.42	27.99	30.92	33.56	31.08	29.26	27.94	31.24	27.89	27.55	30.38
LGSR	**30.50**	**32.28**	**37.98**	**28.72**	**31.31**	**33.76**	**31.19**	**29.99**	**28.21**	**31.61**	**28.14**	**27.89**	**30.96**
	60% pixels missing												
Images	**Cowboy**	**Bear**	**House**	**Lake**	**Leaves**	**Lena**	**Lily**	**Flowers**	**Nanna**	**Agaric**	**Girls**	**Fireman**	**Average**
SALSA [72]	26.99	32.21	32.76	28.14	26.29	31.49	29.65	29.36	26.94	30.08	27.02	27.15	29.01
BPFA [73]	28.42	33.09	36.40	29.75	29.83	33.54	31.35	30.61	28.63	31.60	28.75	28.23	30.85
IPPO [74]	29.58	33.61	38.25	29.30	30.88	34.89	32.17	30.81	29.41	32.89	29.32	29.13	31.69
JSM [75]	28.89	33.10	38.55	29.49	31.47	34.56	31.59	30.52	29.09	32.10	29.01	28.79	31.43
GSR [3]	29.51	33.61	39.68	29.86	33.31	35.78	33.05	31.71	30.09	33.12	29.47	29.34	32.38
Aloha [76]	28.92	32.69	38.68	29.24	31.41	34.72	31.47	30.72	29.51	32.20	28.91	28.24	31.39
NGS [77]	27.78	32.90	36.29	28.68	28.87	32.81	30.53	29.84	28.06	31.12	27.83	27.67	30.20
TSLRA [78]	28.83	32.77	37.23	29.01	30.19	34.26	31.55	30.65	29.17	32.34	28.79	28.73	31.13
JPG-SR [79]	29.57	33.60	39.25	30.05	33.26	35.72	33.09	31.41	30.22	32.93	29.86	29.47	32.37
LGSR	**29.72**	**33.94**	**39.82**	**30.66**	**33.70**	**35.97**	**33.31**	**31.97**	**30.40**	**33.57**	**30.13**	**29.83**	**32.75**
	50% pixels missing												
Images	**Cowboy**	**Bear**	**House**	**Lake**	**Leaves**	**Lena**	**Lily**	**Flowers**	**Nanna**	**Agaric**	**Girls**	**Fireman**	**Average**
SALSA [72]	28.59	33.86	35.17	29.69	28.11	33.08	31.13	30.92	28.53	31.51	28.60	28.54	30.64
BPFA [73]	30.21	34.54	39.24	31.78	32.79	35.61	33.41	32.55	30.68	33.32	30.58	30.12	32.90
IPPO [74]	31.30	35.28	40.02	30.98	33.32	36.50	34.04	32.49	31.17	34.55	31.05	30.82	33.46
JSM [75]	30.75	34.74	40.53	31.18	33.78	36.39	33.46	32.04	30.75	33.94	30.68	30.37	33.22
GSR [3]	31.70	35.62	41.61	32.14	35.86	37.64	35.41	33.48	32.15	35.31	31.93	31.01	34.49
Aloha [76]	30.46	34.29	40.58	31.17	34.01	36.41	33.33	32.40	31.24	33.85	30.59	29.88	33.18
NGS [77]	29.32	34.40	38.85	30.22	31.23	34.56	32.31	31.40	29.71	32.89	29.60	29.22	31.98
TSLRA [78]	30.45	33.01	40.22	30.53	32.56	35.52	33.20	32.04	30.87	33.68	30.48	30.25	32.74
JPG-SR [79]	31.64	35.52	40.85	31.91	35.84	37.40	35.20	33.20	32.27	34.82	31.90	30.96	34.29
LGSR	**31.80**	**35.89**	**41.78**	**32.57**	**36.35**	**37.90**	**35.43**	**33.69**	**32.50**	**35.42**	**32.19**	**31.43**	**34.74**

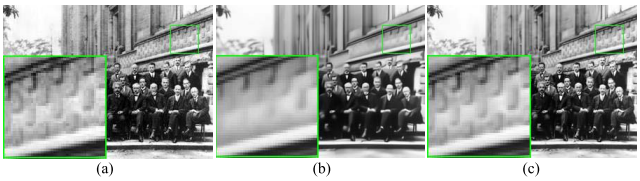

(a) (b) (c)

Fig. 9. (a) Denoising images are obtained by (b) N2N [69] method and (c) our proposed LGSR method.

achieves a better visual perception of both textures and details but also significantly eliminates visual artifacts.

Furthermore, we apply the proposed LGSR to the real image denoising. Due to the unknown noise level for real noisy images, we need to exploit some noise estimation methods to estimate the noise level. To this end, we employ the scheme proposed in [80] to evaluate the noise level. The proposed LGSR is comparable to the N2N method [69], which is a state-of-the-art real image denoising method. Fig. 9 shows an example of real image denoising by comparing N2N with our proposed LGSR method. We can see that the proposed LGSR achieves more image details than the N2N method. Hence, this experiment demonstrates the feasibility of the proposed LGSR algorithm for the real image denoising problem.

B. Image Inpainting

In this section, we employ the proposed LGSR algorithm for image inpainting. We mainly consider that the masks are generated with different partial random samples, including 90%, 80%, 70%, 60%, and 50% pixels missing. The main parameters of the proposed LGSR-based image inpainting algorithm are set as follows. The size of the patch is set to 7×7, and the number of nonlocal similar patches m is set to 60. We empirically set the scale factor $\gamma = 0.001$ and 0.0008 for 90% pixels missing and others, respectively. Two parameters ρ and μ are set to $(1e-5, 1e-5)$, $(3e-5, 2e-5)$, $(1e-5, 3e-5)$, and $(4e-5, 3e-5)$ for 90% pixels missing, 80% pixels missing, 70% pixels missing, and others, respectively. Moreover, for all the cases, σ_n is set to $\sqrt{2}$.

To verify the effectiveness of the proposed LGSR model, we first compare it with some leading methods, including

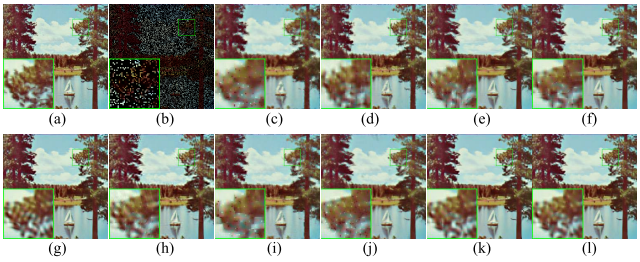

Fig. 10. Image inpainting results on image Lake (80% pixels missing). (a) Original image. (b) Degraded image. (c) SALSA [72] (PSNR = 24.94 dB and SSIM = 0.8036). (d) BPFA [73] (PSNR = 25.82 dB and SSIM = 0.8360). (e) IPPO [74] (PSNR = 25.48 dB and SSIM = 0.8297). (f) JSM [75] (PSNR = 25.82 dB and SSIM = 0.8357). (g) GSR [3] (PSNR = 25.68 dB and SSIM = 0.8559). (h) Aloha [76] (PSNR = 25.32 dB and SSIM = 0.8559). (i) NGS [77] (PSNR = 25.10 dB and SSIM = 0.8180). (j) TSLRA [78] (PSNR = 25.47 dB and SSIM = 0.8184). (k) JPG-SR [79] (PSNR = 25.92 dB and SSIM = 0.8506). (l) LGSR (PSNR = 26.33 dB and SSIM = 0.8611).

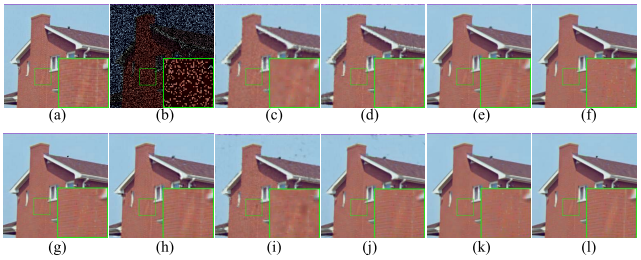

Fig. 11. Image inpainting results on image House (80% pixels missing). (a) Original image. (b) Degraded image. (c) SALSA [72] (PSNR = 29.54 dB and SSIM = 0.8643). (d) BPFA [73] (PSNR = 30.80 dB and SSIM = 0.8929). (e) IPPO [74] (PSNR = 33.65 dB and SSIM = 0.9215). (f) JSM [75] (PSNR = 34.31 dB and SSIM = 0.9103). (g) GSR [3] (PSNR = 35.57 dB and SSIM = 0.9314). (h) Aloha [76] (PSNR = 33.79 dB and SSIM = 0.9276). (i) NGS [77] (PSNR = 31.34 dB and SSIM = 0.8868). (j) TSLRA [78] (PSNR = 32.37 dB and SSIM = 0.9204). (k) JPG-SR [79] (PSNR = 34.99 dB and SSIM = 0.9151). (l) LGSR (PSNR = 35.83 dB and SSIM = 0.9333).

SALSA [72], BPFA [73], IPPO [74], JSM [75], GSR [3], Aloha [76], NGS [77], TSLRA [78], and JPG-SR [79]. What is noteworthy is that all competing methods are using image NSS priors, except for the SALSA method. GSR is an NSS-prior-based baseline method for image inpainting. The TSLRA method exploits a reweighted NNM that attains a superior restoration performance. The JPG-SR method combines patch sparsity and GSR priors to achieve a state-of-the-art inpainting performance. We compare these competing methods by testing 12 natural images, whose scenes are shown in Fig. 4. As can be seen in Table III, our proposed LGSR achieves the best PSNR results than other competing methods. Concretely, on average, our proposed LGSR roughly enhances 3.46, 1.87, 1.06, 1.24, 0.38, 1.31, 2.44, 1.50, and 0.44 dB, compared with SALSA, BPFA, IPPO, JSM, GSR, Aloha, NGS, TSLRA, and JPG-SR, respectively. Some visual comparison results of these competing methods are presented in Figs. 10 and 11. To be concrete, for image Lake in Fig. 10, we can see that SALSA, IPPO, JSM, NGS, and TSLRA methods are apt to over-smooth the images. Meanwhile, BPFA, GSR, Aloha, and JPG-SR methods usually produce some undesirable ring artifacts. For image House in Fig. 11, it can be seen that SALSA, BPFA, JSM, and NGS methods produce the worst visual results. Although IPPO, GSR, and JPG-SR methods achieve better visual results

TABLE IV

AVERAGE PSNR (dB) (TOP ENTRY IN EACH CELL) AND SSIM (BOTTOM ENTRY) RESULTS ARE OBTAINED BY THE PROPOSED LGSR AND THREE DEEP-LEARNING METHODS ON TESTING THE BSD68 DATASET [63]

Methods	90%	80%	70%	60%	Average
IRCNN [10]	24.13	27.42	**29.73**	**31.72**	28.25
	0.6806	0.8158	0.8823	0.9209	0.8249
DIP [11]	24.67	26.96	28.80	30.28	27.68
	0.7135	0.8049	0.8619	0.8883	0.8172
IDBP [81]	24.10	26.95	29.08	30.97	27.78
	0.6954	0.7989	0.8594	0.9009	0.8137
LGSC	**24.85**	**27.60**	29.70	31.58	**28.43**
	0.7321	**0.8332**	**0.8877**	**0.9230**	**0.8440**

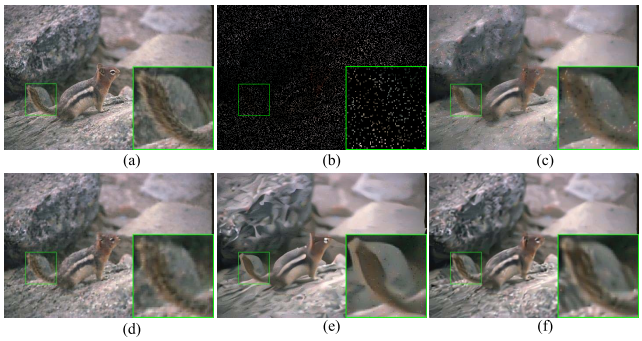

Fig. 12. Image inpainting results on image 123 074 (90% pixels missing). (a) Original image. (b) Degraded image. (c) IRCNN [10] (PSNR = 25.61 dB and SSIM = 0.6812). (d) DIP [11] (PSNR = 27.11 dB and SSIM = 0.7733). (e) IDBP [81] (PSNR = 26.17 dB and SSIM = 0.7136). (f) LGSR (PSNR = 27.38 dB and SSIM = 0.7749).

than SALSA, BPFA, JSM, and NGS methods, they are prone to generate the over-smooth phenomenon. TSLRA is good at capturing repetitive image textures, because it uses a reliable reweighted NNM algorithm, while this method generates some undesirable black pieces. Compared with these competing methods, our proposed LGSR method achieves the best visual result on the whole, which not only preserves image textures and small details but also effectively eliminates the undesirable visual artifacts.

We also compare the proposed LGSR-based image inpainting algorithm with some deep-learning-based image inpainting methods, including IRCNN [10], DIP [11], and IDBP [81]. It is worth noting that they are state-of-the-art CNN-based image inpainting methods with repairing pixels random missing images. We comprehensively evaluate the inpainting performance of these competing methods by testing the BSD68 dataset [63]. According to Table IV, we can observe that our proposed LGSR attains better PSNR and SSIM results in almost all the cases. In particular, our proposed LGSR consistently outperforms other competing methods in terms of SSIM. Specifically, the average SSIM gains of our proposed LGSR over IRCNN, DIP, and IDBP methods are 0.0191, 0.0269, and 0.0304, respectively. The visual comparison results with 90% pixels missing for image 23 074 and image 1 59 008 are presented in Figs. 12 and 13, respectively. It is evident that IRCNN and DIP methods still suffer from noticeable visual artifacts, while the IDBP method is prone to over-smooth the

TABLE V

AVERAGE PSNR (dB) AND SSIM COMPARISON RESULTS ARE OBTAINED BY RCOS [82], GSR [3], JASR [83], ASNR [54], AND THE PROPOSED LGSR METHODS ON TESTING THE BSD68 DATASET [63]

Ratio	Rcos [82]		GSR [3]		JASR [83]		ASNR [54]		**LGSR**	
0.1	26.03	0.7135	25.83	0.7356	26.19	0.7325	26.32	0.7420	**26.33**	**0.7445**
0.2	28.68	0.8067	29.28	0.8408	29.46	0.8317	29.72	0.8471	**29.78**	**0.8489**
0.3	30.62	0.8621	31.82	0.8967	31.63	0.8847	32.10	0.9001	**32.30**	**0.9013**
0.4	32.33	0.8991	34.02	0.9315	33.52	0.9188	34.22	0.9335	**34.32**	**0.9340**
Average	29.42	0.8204	30.24	0.8512	30.20	0.8419	30.59	0.8557	**30.68**	**0.8572**

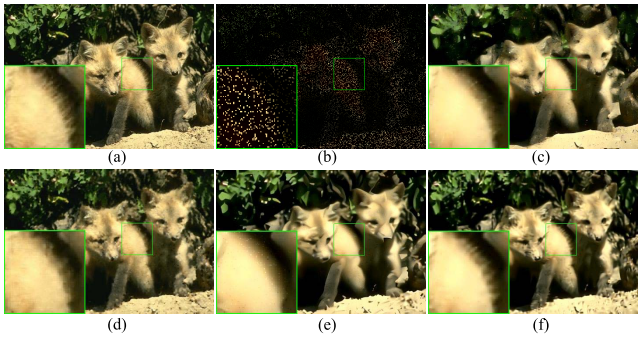

Fig. 13. Image inpainting results on image 159 008 (90% pixels missing). (a) Original image. (b) Degraded image. (c) IRCNN [10] (PSNR = 22.64 dB and SSIM = 0.7013). (d) DIP [11] (PSNR = 23.31 dB and SSIM = 0.7578). (e) IDBP [81] (PSNR = 22.94 dB and SSIM = 0.7286). (f) LGSR (PSNR = 23.89 dB and SSIM = 0.7808).

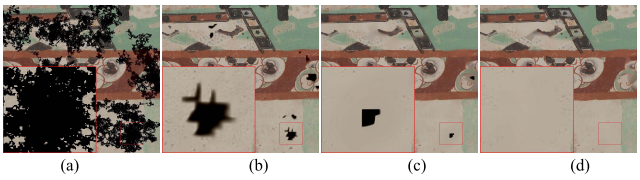

Fig. 14. Image semantic inpainting for historical mural image 1. (a) Degraded image. (b) TSLRA method [78]. (c) IRCNN method [10]. (d) LGSR method.

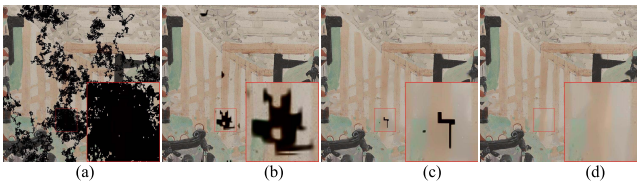

Fig. 15. Image semantic inpainting for historical mural image 2. (a) Degraded image. (b) TSLRA method [78]. (c) IRCNN method [10]. (d) LGSR method.

images, leading to image details missing. By contrast, our proposed LGSR generates much more visually pleasant results than these deep-learning-based image inpainting approaches.

Moreover, our proposed LGSR method can be applied to semantic image inpainting. The proposed LGSR is comparable to TSLRA and IRCNN methods. Note that the TSLRA method can be qualified for various image inpainting tasks, while IRCNN utilizes strong deep priors to obtain a superior performance. We exploit these competing methods to test two historical mural images. As shown in Figs. 14 and 15, the proposed LGSR can effectively reconstruct damaged regions compared with other competing methods.

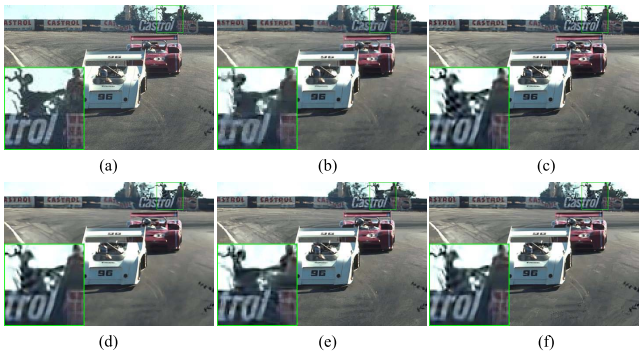

Fig. 16. Image CS results on image 21 077 from the BSD68 dataset [63] (0.2 N CS measurements). (a) Original image. (b) Rcos [82] (PSNR = 28.90 dB and SSIM = 0.8211). (c) GSR [3] (PSNR = 29.04 dB and SSIM = 0.8438). (d) JASR [83] (PSNR = 29.33 dB and SSIM = 0.8217). (e) ASNR [54] (PSNR = 29.26 dB and SSIM = 0.8462). (f) LGSR (PSNR = 29.60 dB and SSIM = 0.8479).

C. Image Compressive Sensing

In this section, we employ the proposed LGSR method to image CS. Similar to [3], [42], in our experiments, we produce the CS measurements at the block level through a Gaussian random projection matrix to test the image, namely, block-based with a block size of 32 × 32. The parameters of our proposed LGSR-based image CS algorithm are set as follows. The patch size $b \times b$ is set to 7 × 7, the number of nonlocal similar patches m is set to 60, and σ_n is set to $\sqrt{2}$. Two parameters ρ and μ are set to $(7e-4, 5e-4)$, $(6e-4, 3e-4)$, $(9e-4, 1e-4)$, and $(6e-4, 3e-4)$ for 0.1, 0.2, 0.3, and 0.4 N CS measurements, respectively.

We first compare the proposed LGSR with four classic methods: Rcos [82], GSR [3], JASR [83], and ASNR [54]. It is worth noting that image NSS priors are all used in these competing methods. GSR is the block-based CS baseline method. ASNR is our previous work that jointly exploits image NSS and sparsity residual priors to achieve a state-of-the-art CS reconstruction performance. Table V lists the average PSNR and SSIM results of these competing methods on testing the BSD68 dataset [63]. It can be seen that our proposed LGSR achieves better quantitative results than other competing methods. To be concrete, the average improvement of the proposed LGSR over Rcos, GSR, JASR, and ASNR methods are 1.27, 0.44, 0.48, and 0.05 dB in PSNR and 0.0368, 0.0060, 0.0153, and 0.0015 in SSIM, respectively. The visual comparison of image 21 077 with 0.2 N measurements for these competing methods is shown in Fig. 16. One can observe that the Rcos method generates the worst visible result, especially it is prone to produce some sandy phenomena. The GSR and

TABLE VI

AVERAGE PSNR (dB) COMPARISON RESULTS ARE OBTAINED BY OUR PROPOSED LGSR WITH FIVE DEEP-LEARNING-BASED CS METHODS ON TESTING THE SET11 DATASET [84]

Methods	0.1	0.3	0.4	0.5	Average
SDA [85]	22.65	26.63	27.79	28.95	26.51
ReconNet [84]	24.28	28.74	30.58	31.50	28.78
IST-Net [86]	25.80	32.91	35.36	37.43	32.88
IST-Net$^+$ [86]	26.64	33.82	36.06	38.07	33.65
CSNet [42]	28.11	33.87	36.13	37.54	33.91
LGSR	**28.24**	**34.93**	**37.10**	**38.99**	**34.82**

(a) (b) (c) (d) (e)

Fig. 17. Image CS results on image Barbara (0.1 N CS measurements). (a) Original image. (b) ReconNet [84] (PSNR = 21.89 dB and SSIM = 0.5732). (c) IST-Net$^+$ [86] (PSNR = 23.61 dB and SSIM = 0.6888). (d) CSNet [42] (PSNR = 24.37 dB and SSIM = 0.7217). (e) LGSR (PSNR = 29.40 dB and SSIM = 0.8886).

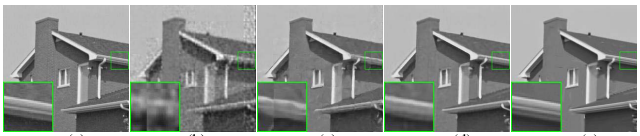

(a) (b) (c) (d) (e)

Fig. 18. Image CS results on image House (0.1 N CS measurements). (a) Original image. (b) ReconNet [84] (PSNR = 25.69 dB and SSIM = 0.6936). (c) IST-Net$^+$ [86] (PSNR = 30.81 dB and SSIM = 0.8388). (d) CSNet [42] (PSNR = 32.36 dB and SSIM = 0.8686). (e) LGSR (PSNR = 34.16 dB and SSIM = 0.8796).

JASR methods produce some unwished ringing artifacts, while some over-smooth effects have existed in JASR. The ANSR method generates some undesirable visual artifacts. By and large, the proposed LGSR achieves better image details and textures than other competing methods.

Recently, deep-learning-based techniques have achieved favorable performance in image CS reconstruction. We now compare our proposed LGSR with several deep-learning-based image CS reconstruction methods, including SDA [85], ReconNet [84], IST-Net [86], IST-Net$^+$ [86], and CSNet [42]. It is worth noting that CSNet jointly optimizes the sampling and reconstruct networks that deliver a state-of-the-art reconstruction performance. We compare these competing methods by testing the Set11 dataset [84], which is still a benchmark dataset for image CS reconstruction. The average PSNR comparison results are provided in Table VI, from which we can see that the proposed LGSR achieves the best PSNR results than other competing methods. The proposed LGSR roughly achieves 8.31, 6.04, 1.94, 1.17, and 0.91 dB improvements over SDA, ReconNet, IST-Net, IST-Net$^+$, and CSNet, respectively. Some visual comparison results of these competing methods are shown in Figs. 17 and 18. We can significantly see that SDA and ReconNet methods still produce staircase artifacts, while CSNet is apt to produce some undesirable visual artifacts. In contrast, our proposed LGSR not only eliminates visual artifacts but also preserves fine image details.

TABLE VII

ABLATION STUDY: AVERAGE PSNR (dB) COMPARISON RESULTS ARE ACHIEVED BY CLASSIC GSR, LR, AND THE PROPOSED LGSR METHODS FOR IMAGE DENOISING ON TESTING THE SET12 DATASET [40]

Methods	10	20	30	40	50	75	100	Average
GSR	34.55	31.02	29.22	27.85	26.96	25.16	23.78	28.36
LR	34.53	31.10	29.17	27.85	26.81	24.95	23.66	28.30
LR-GSC	**34.66**	**31.27**	**29.36**	**28.04**	**27.00**	**25.25**	**23.95**	**28.50**

TABLE VIII

AVERAGE (dB) COMPARISON RESULTS ARE OBTAINED BY LR-GSC [53] AND OUR PROPOSED LGSR METHODS FOR THREE IMAGE RESTORATION TASKS ON TESTING THE BSD68 DATASET [63]

Image Denoising						
Methods	**10**	**20**	**30**	**40**	**50**	**Average**
LR-GSC [53]	34.05	30.26	28.34	27.15	26.30	29.22
LGSR	**34.21**	**30.49**	**28.56**	**27.29**	**26.37**	**29.38**
Image Inpainting						
Methods	**90%**	**80%**	**70%**	**60%**	**50%**	**Average**
LR-GSC [53]	24.84	27.58	29.67	31.52	33.44	29.41
LGSR	**24.85**	**27.60**	**29.70**	**31.58**	**33.50**	**29.45**
Image CS						
Methods	**0.1**	**0.2**	**0.3**	**0.4**	**0.5**	**Average**
LR-GSC [53]	26.29	29.74	32.17	34.28	36.29	31.75
LGSR	**26.33**	**29.78**	**32.30**	**34.32**	**36.33**	**31.81**

D. Ablation Studies

In this section, we conduct several ablation studies to verify the effectiveness of the proposed LGSR model. We first compare the proposed LGSR-based image restoration model (6) with two single-prior-based image restoration models, namely, the GSR model [incorporating (1) into (5)] and the LR model [incorporating (2) into (5)]. Then, we exploit typical GSR, LR, and our proposed LGSR models to the image denoising task, because image denoising is an ideal test bed for image models and is less affected by external factors. In Table VII, we evaluate these competing methods for testing the Set12 dataset [40], from which we can see that our proposed LGSR method achieves better quantitative results than classic GSR and LR models. Accordingly, this ablation study demonstrates that the proposed LGSR model is effective.

Second, the LR-GSC method [63] also jointly uses group sparsity and LR priors to image restoration. However, LR-GSC enforces the LR property to each group coefficient, leading to a suboptimal solution, since each group coefficient cannot guarantee that it has an LR property. We now compare the proposed LGSR with the LR-GSC method and test them on the BSD68 dataset [63] for three image restoration tasks. Table VIII presents the average PSNR comparison results of these two competing methods. We can observe that the proposed LGSR consistently outperforms the LR-GSC method. Therefore, this experiment result further demonstrates the effectiveness of our proposed LGSR model.

E. Convergence

It is challenging to give a theoretical proof for convergence of the proposed algorithm because of the existence of the blocking matching (BM) operator [8], [39]. Therefore, we hereby provide empirical evidence to depict the

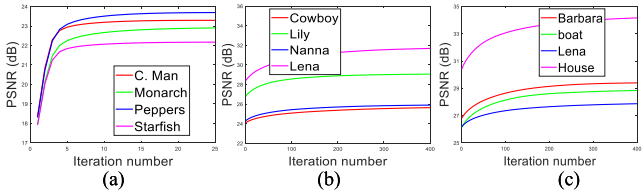

Fig. 19. Convergence behavior of the proposed LGSR algorithm. (a) Convergence of image denoising with $\sigma_n = 100$. (b) Convergence of image inpainting with 80% pixels missing. (c) Convergence of image CS with sampling ratio 0.1 N.

convergence behavior of the proposed LGSR-based image restoration algorithm. Fig. 19 plots the evaluations of PSNR values versus the iteration numbers for image denoising with $\sigma_n = 100$, image inpainting with 80% pixels missing, and image CS with sampling ratio 0.1 N. In both the cases, we can clearly see that with the increase in iteration numbers, the PSNR curves monotonically increase and finally become flat and stable. Hence, our proposed LGSR algorithm enjoys a good convergence property.

VII. Conclusion

Traditional GSR-based image restoration models have imposed only plain sparsity over individual patch of the group in image modeling, and the restoration results are limited by ignoring other beneficial image properties. This article has proposed a novel LGSR model, and its applications into image restoration have been explored. The proposed LGSR has jointly exploited the sparsity and LR priors of the group under a unified framework, which is mutually complementary by preserving image texture and structure information for high-quality image restoration. Moreover, we have developed an alternating minimization algorithm with an adaptively adjusted parameter scheme to solve the proposed optimization problem. Experimental results on three image restoration tasks, including denoising, inpainting, and CS, have demonstrated that the proposed LGSR algorithm outperforms many popular or state-of-the-art methods in both the objective and the perceptual quality.

References

[1] S. Osher, M. Burger, D. Goldfarb, J. Xu, and W. Yin, "An iterative regularization method for total variation-based image restoration," *Multiscale Model., Simul.*, vol. 4, no. 2, pp. 460–489, Jun. 2005.

[2] M. Elad and M. Aharon, "Image denoising via sparse and redundant representations over learned dictionaries," *IEEE Trans. Image Process.*, vol. 15, no. 12, pp. 3736–3745, Dec. 2006.

[3] J. Zhang, D. Zhao, and W. Gao, "Group-based sparse representation for image restoration," *IEEE Trans. Image Process.*, vol. 23, no. 8, pp. 3336–3351, Aug. 2014.

[4] Z. Zha, X. Yuan, B. Wen, J. Zhou, J. Zhang, and C. Zhu, "A benchmark for sparse coding: When group sparsity meets rank minimization," *IEEE Trans. Image Process.*, vol. 29, pp. 5094–5109, 2020.

[5] X. Zhang, X. Li, Z. Tang, S. Zhang, and S. Xie, "Noise removal in embedded image with bit approximation," *IEEE Trans. Knowl. Data Eng.*, early access, May 14, 2020, doi: 10.1109/TKDE.2020.2992572.

[6] W. Dong, G. Shi, and X. Li, "Nonlocal image restoration with bilateral variance estimation: A low-rank approach," *IEEE Trans. Image Process.*, vol. 22, no. 2, pp. 700–711, Feb. 2013.

[7] B. Wen, S. Ravishankar, and Y. Bresler, "Structured overcomplete sparsifying transform learning with convergence guarantees and applications," *Int. J. Comput. Vis.*, vol. 114, nos. 2–3, pp. 137–167, 2015.

[8] S. Gu, L. Zhang, W. Zuo, and X. Feng, "Weighted nuclear norm minimization with application to image denoising," in *Proc. IEEE Conf. Comput. Vis. Pattern Recognit.*, Jun. 2014, pp. 2862–2869.

[9] Z. Zha, X. Yuan, B. Wen, J. Zhou, J. Zhang, and C. Zhu, "From rank estimation to rank approximation: Rank residual constraint for image restoration," *IEEE Trans. Image Process.*, vol. 29, pp. 3254–3269, 2020.

[10] K. Zhang, W. Zuo, S. Gu, and L. Zhang, "Learning deep CNN denoiser prior for image restoration," in *Proc. IEEE Conf. Comput. Vis. Pattern Recognit. (CVPR)*, Jul. 2017, pp. 3929–3938.

[11] V. Lempitsky, A. Vedaldi, and D. Ulyanov, "Deep image prior," in *Proc. IEEE/CVF Conf. Comput. Vis. Pattern Recognit.*, Jun. 2018, pp. 9446–9454.

[12] E. J. Candès, J. Romberg, and T. Tao, "Robust uncertainty principles: Exact signal reconstruction from highly incomplete frequency information," *IEEE Trans. Inf. Theory*, vol. 52, no. 2, pp. 489–509, Feb. 2006.

[13] C. Hou, Y. Jiao, F. Nie, T. Luo, and Z.-H. Zhou, "2D feature selection by sparse matrix regression," *IEEE Trans. Image Process.*, vol. 26, no. 9, pp. 4255–4268, Sep. 2017.

[14] W. Dong, L. Zhang, G. Shi, and X. Li, "Nonlocally centralized sparse representation for image restoration," *IEEE Trans. Image Process.*, vol. 22, no. 4, pp. 1620–1630, Apr. 2013.

[15] Z. Zha, B. Wen, X. Yuan, J. Zhou, C. Zhu, and A. C. Kot, "A hybrid structural sparsification error model for image restoration," *IEEE Trans. Neural Netw. Learn. Syst.*, early access, Feb. 24, 2021, doi: 10.1109/TNNLS.2021.3057439.

[16] R. Dian, S. Li, and L. Fang, "Learning a low tensor-train rank representation for hyperspectral image super-resolution," *IEEE Trans. Neural Netw. Learn. Syst.*, vol. 30, no. 9, pp. 2672–2683, Sep. 2019.

[17] Z. Zha, X. Yuan, B. Wen, J. Zhou, and C. Zhu, "Group sparsity residual constraint with non-local priors for image restoration," *IEEE Trans. Image Process.*, vol. 29, pp. 8960–8975, 2020.

[18] L. Fang, S. Li, X. Kang, and J. A. Benediktsson, "Spectral–spatial hyperspectral image classification via multiscale adaptive sparse representation," *IEEE Trans. Geosci. Remote Sens.*, vol. 52, no. 12, pp. 7738–7749, Dec. 2014.

[19] J. Mairal, F. Bach, J. Ponce, G. Sapiro, and A. Zisserman, "Non-local sparse models for image restoration," in *Proc. IEEE 12th Int. Conf. Comput. Vis.*, Sep. 2009, pp. 2272–2279.

[20] R. Rubinstein, T. Peleg, and M. Elad, "Analysis K-SVD: A dictionary-learning algorithm for the analysis sparse model," *IEEE Trans. Signal Process.*, vol. 61, no. 3, pp. 661–677, Feb. 2013.

[21] A. Buades, B. Coll, and J.-M. Morel, "A non-local algorithm for image denoising," in *Proc. IEEE Comput. Soc. Conf. Comput. Vis. Pattern Recognit. (CVPR)*, vol. 2, Jun. 2005, pp. 60–65.

[22] S. Gu, Q. Xie, D. Meng, W. Zuo, X. Feng, and L. Zhang, "Weighted nuclear norm minimization and its applications to low level vision," *Int. J. Comput. Vis.*, vol. 121, no. 2, pp. 183–208, Jan. 2017.

[23] Z. Zha, X. Yuan, J. Zhou, C. Zhu, and B. Wen, "Image restoration via simultaneous nonlocal self-similarity priors," *IEEE Trans. Image Process.*, vol. 29, pp. 8561–8576, 2020.

[24] W. Dong, G. Shi, Y. Ma, and X. Li, "Image restoration via simultaneous sparse coding: Where structured sparsity meets Gaussian scale mixture," *Int. J. Comput. Vis.*, vol. 114, nos. 2–3, pp. 217–232, 2015.

[25] R. Dian, S. Li, L. Fang, T. Lu, and J. M. Bioucas-Dias, "Nonlocal sparse tensor factorization for semiblind hyperspectral and multispectral image fusion," *IEEE Trans. Cybern.*, vol. 50, no. 10, pp. 4469–4480, Oct. 2020.

[26] J. Xu, L. Zhang, W. Zuo, D. Zhang, and X. Feng, "Patch group based nonlocal self-similarity prior learning for image denoising," in *Proc. IEEE Int. Conf. Comput. Vis. (ICCV)*, Dec. 2015, pp. 244–252.

[27] S. Wang, L. Zhang, and Y. Liang, "Nonlocal spectral prior model for low-level vision," in *Proc. Asian Conf. Comput. Vis.* Springer, 2012, pp. 231–244.

[28] H. Ji, S. Huang, Z. Shen, and Y. Xu, "Robust video restoration by joint sparse and low rank matrix approximation," *SIAM J. Imag. Sci.*, vol. 4, no. 4, pp. 1122–1142, 2011.

[29] H. Zhang, C. Gong, J. Qian, B. Zhang, C. Xu, and J. Yang, "Efficient recovery of low-rank matrix via double nonconvex nonsmooth rank minimization," *IEEE Trans. Neural Netw. Learn. Syst.*, vol. 30, no. 10, pp. 2916–2925, Oct. 2019.

[30] L. Zhang, W. Wei, Q. Shi, C. Shen, A. van den Hengel, and Y. Zhang, "Accurate tensor completion via adaptive low-rank representation," *IEEE Trans. Neural Netw. Learn. Syst.*, vol. 31, no. 10, pp. 4170–4184, Oct. 2020.

[31] H. Liu, E. Li, X. Liu, K. Su, and S. Zhang, "Anomaly detection with kernel preserving embedding," *ACM Trans. Knowl. Discovery Data*, vol. 15, no. 5, pp. 1–18, Oct. 2021.

[32] X. Gong, W. Chen, and J. Chen, "A low-rank tensor dictionary learning method for hyperspectral image denoising," *IEEE Trans. Signal Process.*, vol. 68, pp. 1168–1180, 2020.

[33] H. Liu, X. Li, J. Li, and S. Zhang, "Efficient outlier detection for high-dimensional data," *IEEE Trans. Syst., Man, Cybern., Syst.*, vol. 48, no. 12, pp. 2451–2461, Dec. 2018.

[34] F. Nie, Z. Wang, R. Wang, Z. Wang, and X. Li, "Towards robust discriminative projections learning via non-greedy $\ell_{2,1}$-norm MinMax," *IEEE Trans. Pattern Anal. Mach. Intell.*, vol. 43, no. 6, pp. 2086–2100, Jun. 2021.

[35] Z. Hu, F. Nie, R. Wang, and X. Li, "Low rank regularization: A review," *Neural Netw.*, vol. 136, pp. 218–232, Apr. 2021.

[36] Y. Zhang, Y. Tian, Y. Kong, B. Zhong, and Y. Fu, "Residual dense network for image restoration," *IEEE Trans. Pattern Anal. Mach. Intell.*, vol. 43, no. 7, pp. 2480–2495, Jul. 2021.

[37] Z. Zha, B. Wen, X. Yuan, J. T. Zhou, J. Zhou, and C. Zhu, "Triply complementary priors for image restoration," *IEEE Trans. Image Process.*, vol. 30, pp. 5819–5834, 2021.

[38] S. Li, R. Dian, L. Fang, and J. M. Bioucas-Dias, "Fusing hyperspectral and multispectral images via coupled sparse tensor factorization," *IEEE Trans. Image Process.*, vol. 27, no. 8, pp. 4118–4130, Aug. 2018.

[39] K. Dabov, A. Foi, V. Katkovnik, and K. Egiazarian, "Image denoising by sparse 3-D transform-domain collaborative filtering," *IEEE Trans. Image Process.*, vol. 16, no. 8, pp. 2080–2095, Aug. 2007.

[40] K. Zhang, W. Zuo, Y. Chen, D. Meng, and L. Zhang, "Beyond a Gaussian denoiser: Residual learning of deep CNN for image denoising," *IEEE Trans. Image Process.*, vol. 26, no. 7, pp. 3142–3155, Jul. 2017.

[41] W. Dong, P. Wang, W. Yin, G. Shi, F. Wu, and X. Lu, "Denoising prior driven deep neural network for image restoration," *IEEE Trans. Pattern Anal. Mach. Intell.*, vol. 41, no. 10, pp. 2305–2318, Oct. 2019.

[42] W. Shi, F. Jiang, S. Liu, and D. Zhao, "Image compressed sensing using convolutional neural network," *IEEE Trans. Image Process.*, vol. 29, pp. 375–388, 2020.

[43] R. Dian, S. Li, A. Guo, and L. Fang, "Deep hyperspectral image sharpening," *IEEE Trans. Neural Netw. Learn. Syst.*, vol. 29, no. 11, pp. 5345–5355, Nov. 2018.

[44] X. Wang, R. Girshick, A. Gupta, and K. He, "Non-local neural networks," in *Proc. IEEE/CVF Conf. Comput. Vis. Pattern Recognit.*, Jun. 2018, pp. 7794–7803.

[45] D. Liu, B. Wen, Y. Fan, C. C. Loy, and T. S. Huang, "Non-local recurrent network for image restoration," in *Proc. Adv. Neural Inf. Process. Syst.*, vol. 31, 2018, pp. 1–10.

[46] Y. Zhang, Y. Tian, Y. Kong, B. Zhong, and Y. Fu, "Residual dense network for image super-resolution," in *Proc. IEEE/CVF Conf. Comput. Vis. Pattern Recognit.*, Jun. 2018, pp. 2472–2481.

[47] J. Ma, X.-Y. Liu, Z. Shou, and X. Yuan, "Deep tensor ADMM-Net for snapshot compressive imaging," in *Proc. IEEE/CVF Int. Conf. Comput. Vis. (ICCV)*, Oct. 2019, pp. 10223–10232.

[48] X. Miao, X. Yuan, Y. Pu, and V. Athitsos, "I-Net: Reconstruct hyperspectral images from a snapshot measurement," in *Proc. IEEE/CVF Int. Conf. Comput. Vis.*, Oct. 2019, pp. 4059–4069.

[49] S. Zhang, X. Li, M. Zong, X. Zhu, and R. Wang, "Efficient kNN classification with different numbers of nearest neighbors," *IEEE Trans. Neural Netw. Learn. Syst.*, vol. 29, no. 5, pp. 1774–1785, May 2018.

[50] C. Hou, F. Nie, D. Yi, and D. Tao, "Discriminative embedded clustering: A framework for grouping high-dimensional data," *IEEE Trans. Neural Netw. Learn. Syst.*, vol. 26, no. 6, pp. 1287–1299, Jun. 2015.

[51] S. Zhang, X. Li, M. Zong, X. Zhu, and D. Cheng, "Learning k for kNN classification," *ACM Trans. Intell. Syst. Technol.*, vol. 8, no. 3, pp. 1–19, 2017.

[52] J. Cai, E. J. Candès, and Z. Shen, "A singular value thresholding algorithm for matrix completion," *SIAM J. Optim.*, vol. 20, no. 4, pp. 1956–1982, 2013.

[53] Z. Zha, B. Wen, X. Yuan, J. Zhou, and C. Zhu, "Image restoration via reconciliation of group sparsity and low-rank models," *IEEE Trans. Image Process.*, vol. 30, pp. 5223–5238, 2021.

[54] Z. Zha *et al.*, "Compressed sensing image reconstruction via adaptive sparse nonlocal regularization," *Vis. Comput.*, vol. 34, no. 1, pp. 117–137, 2018.

[55] C. Hou and Z.-H. Zhou, "One-pass learning with incremental and decremental features," *IEEE Trans. Pattern Anal. Mach. Intell.*, vol. 40, no. 11, pp. 2776–2792, Nov. 2018.

[56] J. Zhang, R. Xiong, C. Zhao, Y. Zhang, S. Ma, and W. Gao, "CONCOLOR: Constrained non-convex low-rank model for image deblocking," *IEEE Trans. Image Process.*, vol. 25, no. 3, pp. 1246–1259, Mar. 2016.

[57] C. Hou, L.-L. Zeng, and D. Hu, "Safe classification with augmented features," *IEEE Trans. Pattern Anal. Mach. Intell.*, vol. 41, no. 9, pp. 2176–2192, Sep. 2019.

[58] M. Elad and I. Yavneh, "A plurality of sparse representations is better than the sparsest one alone," *IEEE Trans. Inf. Theory*, vol. 55, no. 10, pp. 4701–4714, Oct. 2009.

[59] W. Dong, L. Zhang, G. Shi, and X. Wu, "Image deblurring and super-resolution by adaptive sparse domain selection and adaptive regularization," *IEEE Trans. Image Process.*, vol. 20, no. 7, pp. 1838–1857, Jul. 2011.

[60] D. L. Donoho, "De-noising by soft-thresholding," *IEEE Trans. Inf. Theory*, vol. 41, no. 3, pp. 613–627, May 1995.

[61] S. Boyd, N. Parikh, and E. Chu, *Distributed Optimization and Statistical Learning Via the Alternating Direction Method of Multipliers*. Delft, The Netherlands: Now Publishers, 2011.

[62] M. Avriel, *Nonlinear Programming: Analysis and Methods*. Chelmsford, MA, USA: Courier Corporation, 2003.

[63] P. Arbeláez, M. Maire, C. Fowlkes, and J. Malik, "Contour detection and hierarchical image segmentation," *IEEE Trans. Pattern Anal. Mach. Intell.*, vol. 33, no. 5, pp. 898–916, Aug. 2011.

[64] D. Zoran and Y. Weiss, "From learning models of natural image patches to whole image restoration," in *Proc. Int. Conf. Comput. Vis.*, Nov. 2011, pp. 479–486.

[65] J. Pang and G. Cheung, "Graph Laplacian regularization for image denoising: Analysis in the continuous domain," *IEEE Trans. Image Process.*, vol. 26, no. 4, pp. 1770–1785, Apr. 2017.

[66] Z. Wang, A. C. Bovik, H. R. Sheikh, and E. P. Simoncelli, "Image quality assessment: From error visibility to structural similarity," *IEEE Trans. Image Process.*, vol. 13, no. 4, pp. 600–612, Apr. 2004.

[67] Y. Blau and T. Michaeli, "The perception-distortion tradeoff," in *Proc. IEEE/CVF Conf. Comput. Vis. Pattern Recognit.*, Jun. 2018, pp. 6228–6237.

[68] Y. Chen and T. Pock, "Trainable nonlinear reaction diffusion: A flexible framework for fast and effective image restoration," *IEEE Trans. Pattern Anal. Mach. Intell.*, vol. 39, no. 6, pp. 1256–1272, Aug. 2017.

[69] J. Lehtinen *et al.*, "Noise2Noise: Learning image restoration without clean data," in *Proc. Int. Conf. Mach. Learn.*, 2018, pp. 2965–2974.

[70] Y. Quan, M. Chen, T. Pang, and H. Ji, "Self2Self with dropout: Learning self-supervised denoising from single image," in *Proc. IEEE/CVF Conf. Comput. Vis. Pattern Recognit. (CVPR)*, Jun. 2020, pp. 1890–1898.

[71] A. Krizhevsky, I. Sutskever, and G. E. Hinton, "ImageNet classification with deep convolutional neural networks," in *Proc. Adv. Neural Inf. Process. Syst.*, vol. 25, 2012, pp. 1097–1105.

[72] M. V. Afonso, J. M. Bioucas-Dias, and M. A. T. Figueiredo, "An augmented Lagrangian approach to the constrained optimization formulation of imaging inverse problems," *IEEE Trans. Image Process.*, vol. 20, no. 3, pp. 681–695, Mar. 2011.

[73] M. Zhou *et al.*, "Nonparametric Bayesian dictionary learning for analysis of noisy and incomplete images," *IEEE Trans. Image Process.*, vol. 21, no. 1, pp. 130–144, Jan. 2012.

[74] I. Ram, M. Elad, and I. Cohen, "Image processing using smooth ordering of its patches," *IEEE Trans. Image Process.*, vol. 22, no. 7, pp. 2764–2774, Jul. 2013.

[75] J. Zhang, D. Zhao, R. Xiong, S. Ma, and W. Gao, "Image restoration using joint statistical modeling in a space-transform domain," *IEEE Trans. Circuits Syst. Video Technol.*, vol. 24, no. 6, pp. 915–928, Jun. 2014.

[76] K. H. Jin and J. C. Ye, "Annihilating filter-based low-rank Hankel matrix approach for image inpainting," *IEEE Trans. Image Process.*, vol. 24, no. 11, pp. 3498–3511, Nov. 2015.

[77] H. Liu, R. Xiong, X. Zhang, Y. Zhang, S. Ma, and W. Gao, "Nonlocal gradient sparsity regularization for image restoration," *IEEE Trans. Circuits Syst. Video Technol.*, vol. 27, no. 6, pp. 1909–1921, Sep. 2016.

[78] Q. Guo, S. Gao, X. Zhang, Y. Yin, and C. Zhang, "Patch-based image inpainting via two-stage low rank approximation," *IEEE Trans. Vis. Comput. Graphics*, vol. 24, no. 6, pp. 2023–2036, Jun. 2018.

[79] Z. Zha, X. Yuan, B. Wen, J. Zhang, J. Zhou, and C. Zhu, "Image restoration using joint patch-group-based sparse representation," *IEEE Trans. Image Process.*, vol. 29, pp. 7735–7750, 2020.

[80] J. Immerkær, "Fast noise variance estimation," *Comput. Vis. Image Understand.*, vol. 64, no. 2, pp. 300–302, Sep. 1996.

[81] T. Tirer and R. Giryes, "Image restoration by iterative denoising and backward projections," *IEEE Trans. Image Process.*, vol. 28, no. 3, pp. 1220–1234, Mar. 2019.

[82] J. Zhang, D. Zhao, C. Zhao, R. Xiong, S. Ma, and W. Gao, "Image compressive sensing recovery via collaborative sparsity," *IEEE J. Emerg. Sel. Topics Circuits Syst.*, vol. 2, no. 3, pp. 380–391, Sep. 2012.

[83] N. Eslahi and A. Aghagolzadeh, "Compressive sensing image restoration using adaptive curvelet thresholding and nonlocal sparse regularization," *IEEE Trans. Image Process.*, vol. 25, no. 7, pp. 3126–3140, May 2016.

[84] K. Kulkarni, S. Lohit, P. Turaga, R. Kerviche, and A. Ashok, "ReconNet: Non-iterative reconstruction of images from compressively sensed measurements," in *Proc. IEEE Conf. Comput. Vis. Pattern Recognit. (CVPR)*, Jun. 2016, pp. 449–458.

[85] A. Mousavi, A. B. Patel, and R. G. Baraniuk, "A deep learning approach to structured signal recovery," in *Proc. 53rd Annu. Allerton Conf. Commun., Control, Comput. (Allerton)*, Sep. 2015, pp. 1336–1343.

[86] J. Zhang and B. Ghanem, "ISTA-Net: Interpretable optimization-inspired deep network for image compressive sensing," in *Proc. IEEE Conf. Comput. Vis. Pattern Recognit.*, Jun. 2018, pp. 1828–1837.

Zhiyuan Zha (Member, IEEE) received the Ph.D. degree from the School of Electronic Science and Engineering, Nanjing University, Nanjing, China, in 2018.

He is currently a Research Fellow with Nanyang Technological University, Singapore. His current research interests include inverse problems in image/video processing, sparse signal representation, and machine learning.

Dr. Zha was a recipient of the Platinum Best Paper Award and the Best Paper Runner Up Award at the IEEE International Conference on Multimedia and Expo in 2017 and 2020, respectively.

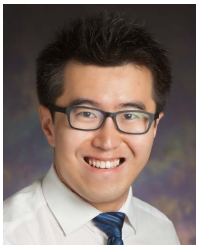

Bihan Wen (Member, IEEE) received the B.Eng. degree in electrical and electronic engineering from Nanyang Technological University, Singapore, in 2012, and the M.S. and Ph.D. degrees in electrical and computer engineering from the University of Illinois at Urbana-Champaign, Champaign, IL, USA, in 2015 and 2018, respectively.

He is currently a Nanyang Assistant Professor with the School of Electrical and Electronic Engineering, Nanyang Technological University. His research interests include machine learning, computational imaging, computer vision, image and video processing, and big data applications.

Dr. Wen was a recipient of the 2016 Yee Fellowship and the 2012 Professional Engineers Board Gold Medal. He was also a recipient of the Best Paper Runner Up Award at the IEEE International Conference on Multimedia and Expo in 2020. He has been an Associate Editor of IEEE TRANSACTIONS ON CIRCUITS AND SYSTEMS FOR VIDEO TECHNOLOGY since 2022. He has also served as a Guest Editor for *IEEE Signal Processing Magazine* in 2022.

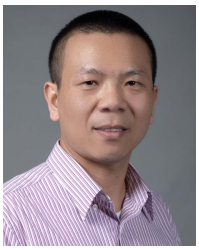

Xin Yuan (Senior Member, IEEE) received the B.Eng. and M.Eng. degrees from Xidian University, Xi'an, China, in 2007 and 2009, respectively, and the Ph.D. degree from The Hong Kong Polytechnic University, Hong Kong, in 2012.

He was a Video Analysis and Coding Lead Researcher with Bell Labs, Murray Hill, NJ, USA, from 2015 to 2021. Prior to this, he was a Post-Doctoral Associate with the Department of Electrical and Computer Engineering, Duke University, Durham, NC, USA, from 2012 to 2015, where he was working on compressive sensing and machine learning. He is currently an Associate Professor with Westlake University, Hangzhou, Zhejiang, China.

Dr. Yuan was a recipient of the Best Paper Runner Up Award at the IEEE International Conference on Multimedia and Expo in 2020. He has been an Associate Editor of *Pattern Recognition* since 2019. He is leading the Special Issue of "Deep Learning for High-Dimensional Sensing" in the IEEE JOURNAL OF SELECTED TOPICS IN SIGNAL PROCESSING in 2021.

Jiantao Zhou (Senior Member, IEEE) received the B.Eng. degree from the Department of Electronic Engineering, Dalian University of Technology, Dalian, China, in 2002, the M.Eng. degree from the Department of Radio Engineering, Southeast University, Dhaka, Bangladesh, in 2005, and the Ph.D. degree from the Department of Electronic and Computer Engineering, The Hong Kong University of Science and Technology, Hong Kong, in 2009.

He held various research positions at the University of Illinois at Urbana-Champaign, Champaign, IL, USA, The Hong Kong University of Science and Technology, Hong Kong, and McMaster University, Hamilton, ON, Canada. He is currently an Associate Professor with the Department of Computer and Information Science, Faculty of Science and Technology, University of Macau, Taipa, Macau. He holds four granted U.S. patents and two granted Chinese patents. His research interests include multimedia security and forensics, and multimedia signal processing.

Dr. Zhou has coauthored three papers that received the Best Paper Award from the IEEE Pacific-Rim Conference on Multimedia in 2007, and the Best Student Paper Award and the Best Paper Runner Up Award from the IEEE International Conference on Multimedia and Expo in 2016 and 2020, respectively. He has been an Associate Editor of IEEE TRANSACTIONS ON IMAGE PROCESSING since 2018 and IEEE TRANSACTIONS ON MULTIMEDIA since 2021.

Ce Zhu (Fellow, IEEE) received the B.S. degree from Sichuan University, Chengdu, China, in 1989, and the M.Eng. and Ph.D. degrees from Southeast University, Nanjing, China, in 1992 and 1994, respectively, all in electronic and information engineering.

He held a Post-Doctoral Research position at The Chinese University of Hong Kong, Hong Kong, in 1995, the City University of Hong Kong, Hong Kong, and the University of Melbourne, Melbourne, VIC, Australia, from 1996 to 1998. He was with Nanyang Technological University, Singapore, for 14 years, from 1998 to 2012, where he was a Research Fellow, a Program Manager, an Assistant Professor, and then was promoted to an Associate Professor in 2005. He has been with the University of Electronic Science and Technology of China, Chengdu, as a Professor, since 2012. His research interests include video coding and communications, video analysis and processing, 3-D video, visual perception, and applications.

Dr. Zhu has served on the editorial boards of a few journals, including as an Associate Editor of IEEE TRANSACTIONS ON IMAGE PROCESSING, IEEE TRANSACTIONS ON CIRCUITS AND SYSTEMS FOR VIDEO TECHNOLOGY, IEEE TRANSACTIONS ON BROADCASTING, and IEEE SIGNAL PROCESSING LETTERS, an Editor of IEEE COMMUNICATIONS SURVEYS AND TUTORIALS, and an Area Editor of *Signal Processing: Image Communication*. He has also served as a Guest Editor of a few special issues in international journals, including as a Guest Editor of the IEEE JOURNAL OF SELECTED TOPICS IN SIGNAL PROCESSING. He was an IEEE Distinguished Lecturer of Circuits and Systems Society from 2019 to 2020. He has been an APSIPA Distinguished Lecturer since 2021.

Alex Chichung Kot (Fellow, IEEE) has been with Nanyang Technological University, Singapore, since 1991. He headed the Division of Information Engineering at the School of Electrical and Electronic Engineering, for 11 years. He has served as an Associate Chair/Research and the Vice Dean Research for the School of Electrical and Electronic Engineering and eight years as an Associate Dean for the College of Engineering. He is currently a Professor and the Director of the Rapid-Rich Object SEarch (ROSE) Laboratory, Singapore, and the NTU-PKU Joint Research Institute, Singapore. He has published extensively in the areas of signal processing for communication, biometrics, image forensics, information security and computer vision, and machine learning.

Dr. Kot is also a fellow of IES and the Academy of Engineering, Singapore. He received the Best Teacher of the Year Award. He is the coauthor for several Best Paper Awards, including ICPR, IEEE WIFS, and IWDW. He has served the IEEE SP Society in various capacities, such as the General Co-Chair for the 2004 IEEE International Conference on Image Processing and the Vice-President for the IEEE Signal Processing Society. He has served as an Associate Editor for more than ten journals, mostly for IEEE TRANSACTIONS. He was elected as the IEEE Distinguished Lecturer for the Signal Processing Society and the Circuits and Systems Society.